Deliverable D 3.6
Model of the non-linear behaviour of masonry at high temperature

Document type	**Deliverable D 3.6**
Document Version / Status	**1.10**
Primary Authors	**João Pereira, jpereira@civil.uminho.pt, UMINHO**
Distribution Level	**PU (Public)**
Project Acronym	**ATHOR**
Project Title	**Advanced THermomechanical multiscale mOdelling of Refractory linings**
Grant Agreement Number	**764987**
Project Website	www.etn-athor.eu
Project Coordinator	**Marc Huger, marc.huger@unilim.fr, UNILIM**
Document Contributors	**João Pereira, jpereira@civil.uminho.pt, UMINHO** **Alain Gasser, alain.gasser@univ-orleans.fr,UORL** **Mahmoud Ali, mahmoud.ali@univ-orleans.fr, UORL** **Pratik Gajjar, pratik.gajjar@civil.uminho.pt, UMINHO** **Thais Soares, thais.soares@civil.uminho.pt, UMINHO**

History of Changes

Version	Date	Author (Organization)	Change	Page
1.0	26.09.2021	Mahmoud ALI (UORL)	Homogenization approach	All
1.1	27.09.2021	Pratik GAJJAR (UMinho) Thais SOARES (UMinho)	Micro-modelling approach	All
1.2	29.09.2021	João Pereira (UMINHO)	Review	All
1.3	30.09.2021	Pratik GAJJAR (UMinho) Thais SOARES (UMinho)	Revision	All
1.4	01.10.2021	Alain GASSER (UORL)	Review	All
1.5	05.10.2021	Pratik GAJJAR (UMinho) Thais SOARES (UMinho)	Revision	All
1.6	12.10.2021	Mahmoud ALI (UORL)	Revision	All
1.7	14.10.2021	Glyn Derrick (UNILIM)	Formatting and English check	All
1.8	20.10.2021	Thais SOARES (UMinho) Mahmoud ALI (UORL)	Revision	1 - 16
1.9	20.10.2021	Marc Huger (UNILIM) Glyn Derrick (UNILIM)	Final check	All
1.10	10.11.2021	Pratik GAJJAR (UMinho) Thais SOARES (UMinho)	Final modifications	17, 28, 32

TABLE OF CONTENTS

1 Introduction

This report will gather the numerical results regarding the non-linear behaviour of masonry (subsystem scale). The data from the experimental thermomechanical campaigns are used to calibrate advanced numerical multiphysics models. Within this document, two different modelling approaches are used: a) homogenization (UORL); and b) micro-modelling (UMINHO). All developed models are compared with experimental results obtained within ATHOR which have already been described in *Deliverable D4.3 - Thermomechanical characterization of subsystems*.

2 Materials

Refractory masonry walls built with alumina spinel cuboid bricks are studied in the present work. The bricks were produced by RHI-Magnesita. They have been fully characterized within the ATHOR network. The chemical composition of the material is 94 wt % alumina, 5 wt % magnesia and 1 wt % other oxides such as iron oxide and silica. The apparent porosity and density of the material are 19 % and 3.13 g/cm^3, respectively [1]. The thermal conductivity and specific heat of the material properties are shown in Figure 1-a and b [2]. The Young's modulus, measured using the ultra-sound technique [3] and mechanical tests, and the ultimate compressive stress [4] variations with temperature are presented in Figure 1- c and d, respectively. The values of Young's modulus measured using mechanical tests are preferred and will be used later in the present work while developing the numerical models.

The masonry walls were built with half and full cuboid bricks. The dimensions of the full bricks are 150×100×140 mm^3 (length, height and depth) and the dimensions of the half bricks are 75×100×140 mm^3. The dimensional tolerances of the bricks are ±2 mm in the pressing direction (150 ± 2 mm) and ±1 mm in directions perpendicular to the pressing direction (100 ± 1 mm and 140 ± 1 mm). The dimensional tolerances result in shape mismatches of the bricks leading to non-uniform joint thickness in the wall and partial initial contact between bricks. As can be seen in Figure 2, the dry joints are almost closed in some locations while being open in other locations.

European Commission
Horizon 2020
European Union funding
for Research & Innovation

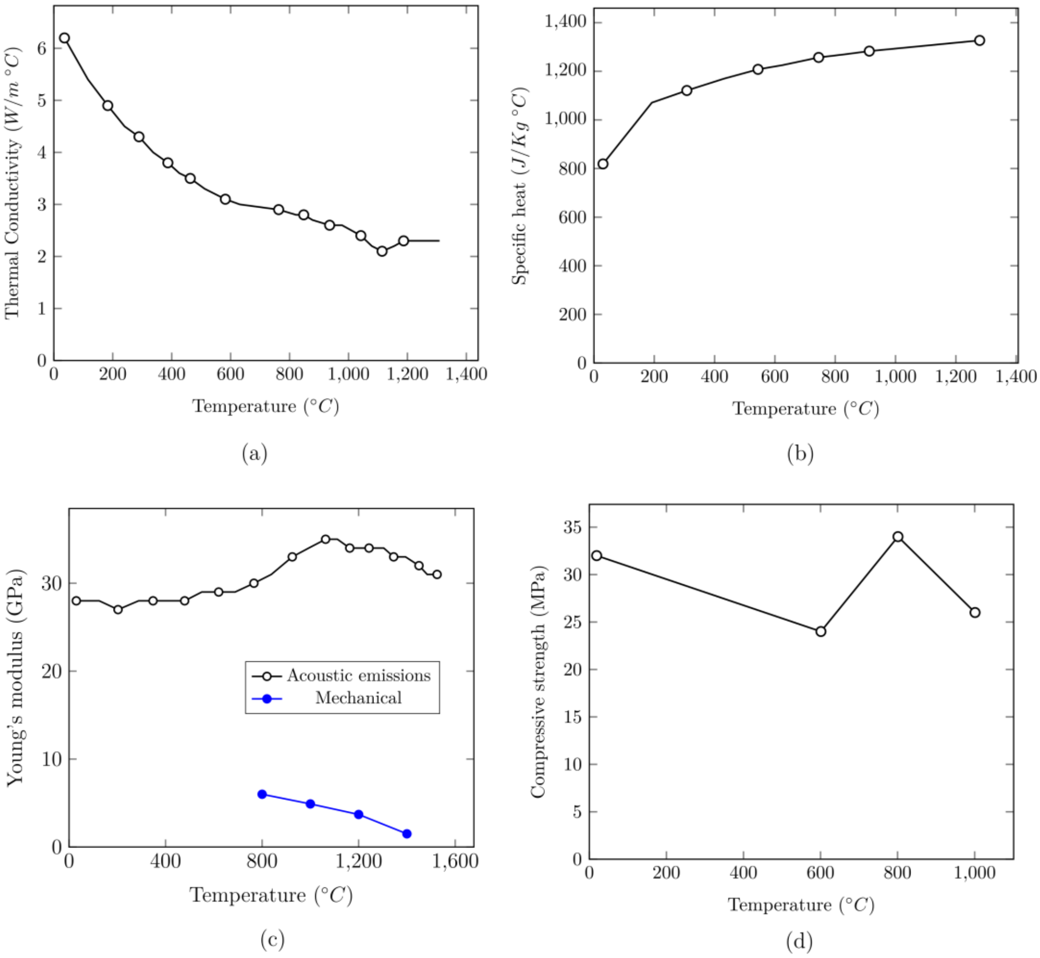

Figure 1: Thermal and mechanical properties of alumina spinel bricks tested and simulated in the present work: (a) thermal conductivity, (b) specific heat, (c) Young's modulus and (d) ultimate compressive strength.

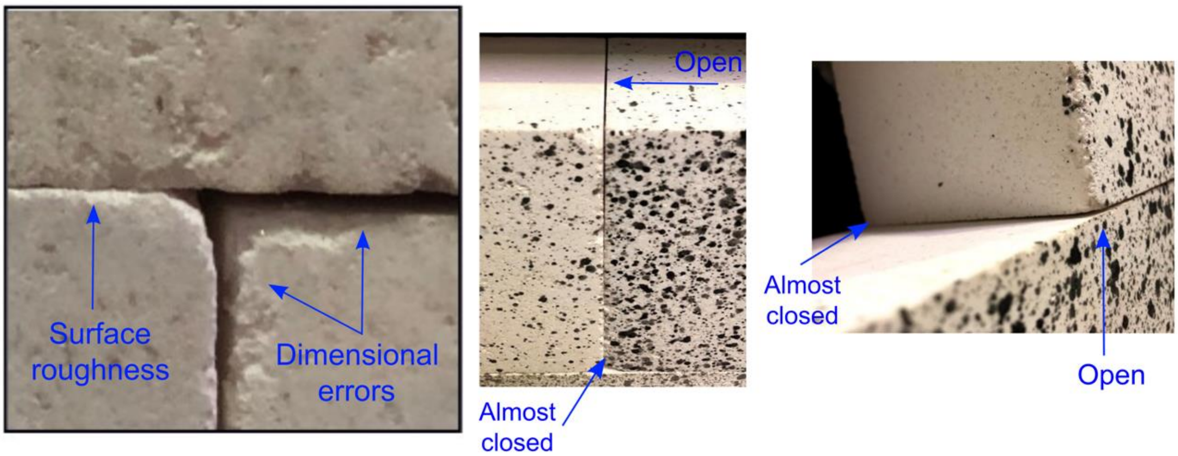

Figure 2: Non-uniform dry joints thickness and partial initial contact, caused by the dimensional tolerances of the bricks.

3 Modelling approaches

As masonry structures are composed of blocks and joints, they feature a great variety of different component materials, geometry, and textures, implying a great number of descriptive parameters, thus, presenting itself as a complex research field [5]. Hence, the importance of sophisticated numerical tools, capable of predicting the behaviour of the structure from the linear stage, through cracking and degradation until complete loss of strength [6]. However, only in the 1990s did the masonry research community begin to show interest in sophisticated numerical tools to study masonry as an opposition to the prevailing tradition of rules-of-thumb and empirical formulae [6].

As a composite material, masonry has certain particularities that complicate the adoption of existing numerical tools from more advanced research fields, such as mechanics of concrete, rock, and composite materials. Hence the necessity for different approaches. Due to the heterogeneous states of stress and strain on a masonry structure, it would be useful to assess the local behaviour of the masonry with mortar through a micro-model. The mechanical properties of both the unit and mortar and the interface between them could then be considered (Figure 3-a). This approach, however, is only adequate for small structural elements. Alternatively, a simplified micro-modelling approach Figure 3-b) can be adopted to address the disadvantages of the detailed micro approach. In the simplified approach, the units are expanded by adding the mortar thickness, the expanded units are modelled as a series of continuum elements and the interaction between the expanded units is modelled as series of discontinuum elements. In case of large analyses, the knowledge of the interaction between units and mortar is, generally, negligible for the global structural behaviour. Therefore, a different approach, denoted macro-modelling, can be used. In this approach, the material is regarded as an anisotropic composite and a relation is established between average masonry strains and average masonry stresses (Figure 3-c). This is a phenomenological approach, meaning that the material parameters must be performed in masonry tests of sufficiently large size under homogeneous states of stress. A complete macro-model must reproduce an orthotropic material with different tensile and compressive strengths along the material axes, as well as different inelastic behaviour for each material axis [6].

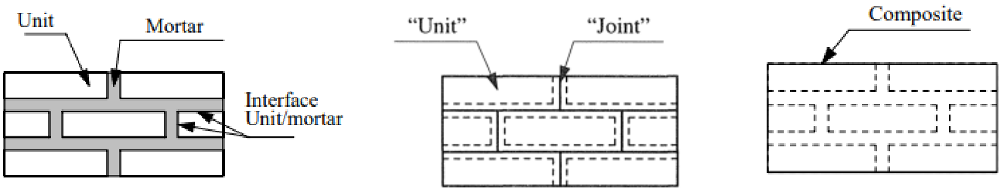

(a) (b) (c)

Figure 3: Modelling strategies for masonry structures
(a) detailed micro-modelling; (b) simplified micro-modelling; (c) macro-modelling [2].

3.1 Micro-modelling approach used at UMINHO

As the wear lining of the steel ladle is built with mortarless masonry, a simplified micro-modelling approach is adopted here. In it, the spatial discretization of the masonry is performed at the level of brick elements, and the dry joints are represented by their contact behaviour using interface elements. Herein, brick elements are simulated with corresponding mechanical parameters of the material from which they are made, and their connection with contact elements that permit separation, penetration, and sliding at the contact.

The micro-modelling approach, in which the units and mortar are modelled as continuum elements and the interfaces between bricks and mortar (or between bricks and bricks) are represented by discontinuous elements. Even though accurate results are obtained using the micro-modelling technique, there is a significant drawback, the large computational resources required to run the analysis [7], [8]. Nevertheless, this approach provides detailed results on the behaviour of the bricks and joints and, therefore, was adopted in this study. The numerical analyses for this approach are performed using the finite element software DIANA FEA [9] and Abaqus [10]. These pieces of software contain an extensive multi-purpose finite element software package that can be utilised in a wide range of engineering sectors.

For the brick elements, several existing material modes might be used. The simplest one is linear elasticity, which is not able to represent certain particularities of the refractory behaviour, but nonetheless is capable of reproducing the expected results within delimitated applications. Another possibility is the concrete damage plasticity (CDP) model, which assumes that failure under compressive crushing and tensile cracking is defined by damage plasticity, using the concept of isotropic damage evolution to represent the inelastic behaviour of concrete like materials. The CDP model is a modification of the Drucker-Prager model [11], [12], however the failure surface's shape, in the deviatory plane, does not need to be a circle. Finally, total strain crack models might also be used. This model is developed along the lines of the Modified Compression Field Theory, originally proposed by Vecchio & Collins [13], and like the multi-directional fixed crack model, the total strain-based crack models follow a smeared approach for the fracture energy.

The total strain crack model is developed along the lines of the Modified Compression Field Theory, originally proposed by Vecchio & Collins [13]. Like the multi-directional fixed crack model, the total strain-based crack models follow a smeared approach for the fracture energy. The three-dimensional extension to this theory is proposed by Selby & Vecchio [14], which theoretical description was followed during the implementation in DIANA. This model is available for concrete and masonry materials in DIANA, with different options for the behaviour in tension and compression. The tensile behaviour can be modelled using different approaches, one resulting in a more complex description than the other [9]. Here, a linear softening curve based on the fracture energy is used to define the behaviour. Concrete-like materials subjected to compressive stresses show a pressure-dependent behaviour, i.e., the strength and ductility increase with increasing isotropic stress. Due to the lateral confinement, the compressive stress-strain relation is modified to incorporate the effects of the increased isotropic stress. Furthermore, it is assumed that the compressive behaviour is influenced by lateral cracking [9]. The response of the material to uniaxial loading in tension and compression is shown in Figure 4.

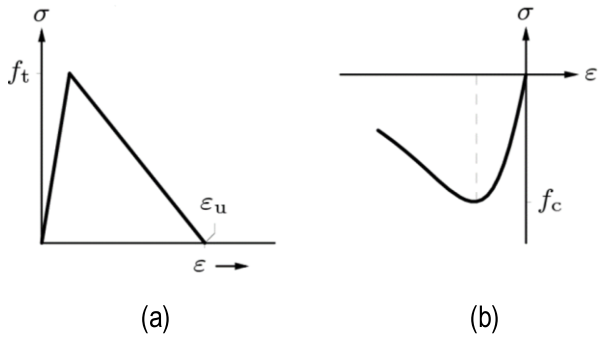

Figure 4: Response of the material to uniaxial loading in: (a) tension and (b) compression [9].

The behaviour of dry-stacked masonry is greatly impacted by the presence of joints. The interface elements used to represent the dry-joints permit discontinuities in the displacement field, and their behaviour is described in terms of a relationship between the tractions or stresses, t, and relative displacements, Δu, across the interface [15]. For the case of two-dimensional interfaces, illustrated in Figure 5, the variables are the stress vector $t = \{t_n, t_t\}$ and the relative displacement $\Delta u = \{\Delta u_n, \Delta u_t\}$, with n and t denoting the normal and tangential (shear) components, respectively [9].

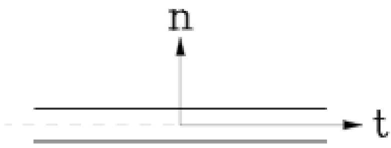

Figure 5: 2D interface axes [9].

The linear elastic relation between these generalized stresses and strains can be written in the standard form as shown in Equation 1.

$$\dot{t} = D\ \Delta\dot{u}$$ **Equation 1**

Where D, the elastic stiffness matrix, is given by $D = diag\{k_n, k_t\}$. k_n sets the relation between the normal stress t_n and the normal relative displacement Δu_n. k_t sets the relation between the shear stress t_t and the shear relative displacement Δu_t. Alternatively, to the linear stiffness, nonlinear elastic stiffness properties may be defined. The available nonlinear elastic model sets a multilinear relation between normal traction and perpendicular relative displacement or between the shear stress and the tangential relative displacement or both [9].

The interface elements were modelled using plane interface elements Q24IF. To simulate interface behaviour, a model for nonlinear elasticity is used. In it, the joints' normal behaviour is represented by a normal stress-normal relative displacement relation. According to Ngapeya et al. [7], increasing the height and length of the wall statistically reduces its effective section (where contact occurs). Therefore, different relations were used to represent masonry with different dimensions. The tangential behaviour is represented by the shear stress-shear relative displacement diagram, which is obtained from the application of the Coulomb criterion [16], defined in Equation 2, where c is the shear strength at zero vertical load stress (usually denoted by cohesion) and μ is the friction coefficient or tangent of the friction angle. For dry joints, the cohesion is zero. The friction coefficient of the alumina bricks as a function of the temperature was obtained by Oliveira et al. [4], here a constant value of 0.6 was applied. Thus, from the normal behaviour curve, considering the same behaviour in tension and compression, it is possible to obtain the definition for the tangential behaviour. The average curves for each geometry are presented in Figure 6.

$$\tau = c + \mu\sigma \qquad \text{Equation 2}$$

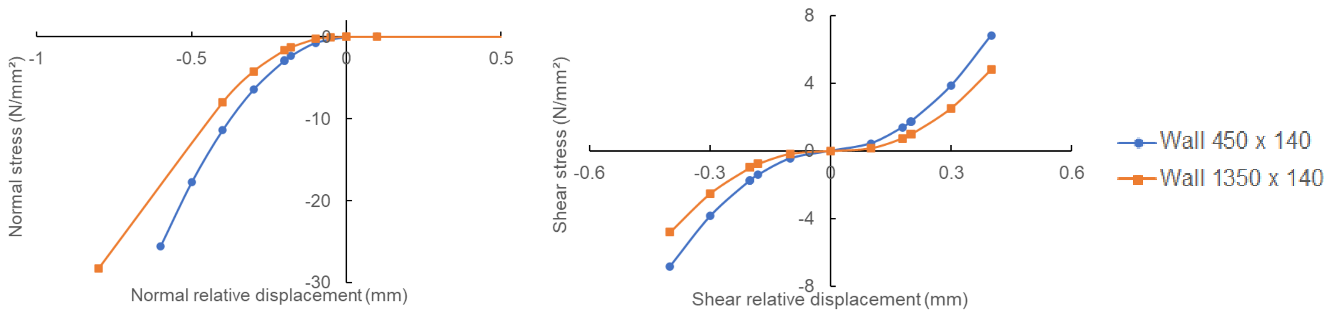

Figure 6: Contact pressure-overclosure relations used for different wall dimensions (a) Normal direction and (b) Shear direction.

3.2 Homogenization approach at UORL

The working linings of the steel ladles studied in this work are built using refractory masonry with dry joints (see Figure 7). The height and diameter of a typical industrial steel ladle are around 5 and 4.5 m, respectively. The working lining is built up from thousands of tapered refractory bricks. In this study, only flat refractory linings are considered, to compare with the developed experimental campaigns. The bricks are periodically arranged in running bond texture. Dry joints with initial thickness (g_0) are separating the bricks from each other. Often, these joints are resulting from the shape, dimensional tolerances and surface unevenness of the bricks. However, sometimes, such as for rotary kilns and blast furnaces, the joints are designed by attaching cardboard spacers to the bricks during the installation to compensate for thermal expansion effects.

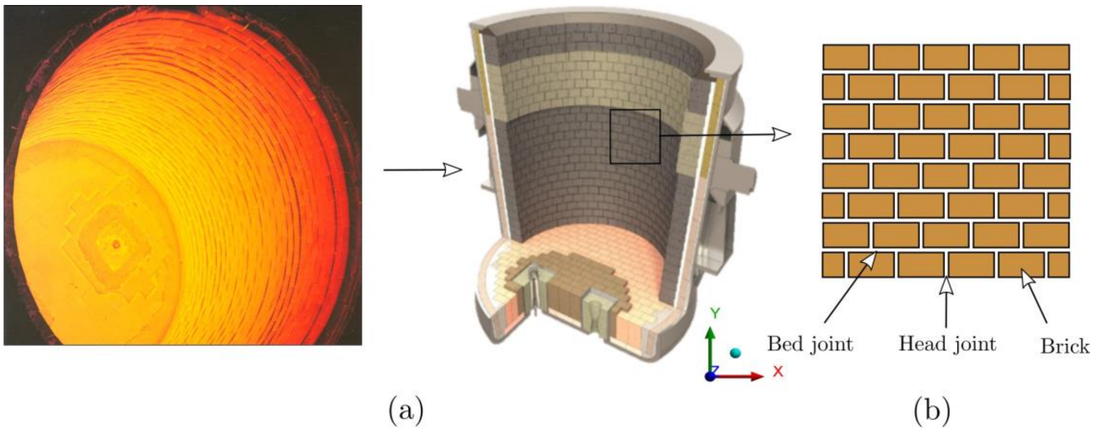

Figure 7: (a) Steel ladle lined with refractory masonry with dry joints [5], and, (b) Schematic of masonry wall with dry joints showing the bricks and the gaps between them.

Two types of joints are defined on the basis of their orientation: bed joints with the initial thickness $g_{0,bed}$ (horizontal joints in Figure 7-b) and head joints with initial thickness $g_{0,head}$ (vertical joints in Figure 7-b). As previously presented in *Deliverable D4.3*, under cyclic loading and unloading, these joints can close and reopen. The mechanical response of masonry with dry joints varies with the closure and reopening of these joints. The experimental results presented in *Deliverable D4.3* show that the effective stiffness of the masonry walls increases with the closure of joints. This phenomenon should be considered when developing thorough numerical models for the simulation of masonry with dry joints.

For the purpose of considering the impact of joints closure and reopening on the homogenized elastic-viscoplastic behaviour of masonry structures, four possible joint patterns are predefined (see Figure 8). Each pattern is based on the state of both bed and head joints (i.e., open or closed) and represents different periodic masonry structures with different equivalent behaviours. The four joint patterns are as follows [8], [17]–[19]:

1. Pattern C: head and bed joints are Closed (all joints are closed).
2. Pattern B: Bed joints are closed, while head joints are open.
3. Pattern H: Head joints are closed, while bed joints are open.
4. Pattern O: head and bed joints are Open (all joints are open).

Further details on the nonlinear homogenization analysis and the identification of the homogenized elastic viscoplastic behaviour of the four patterns and the transition criteria from one joint pattern to another are described in detail in references [8], [18].

The orthotropic homogenized elastic behaviour of the four joint patterns can be described using the orthotropic forms of Hooke's law as [8], [18]:

$$\bar{\bar{\Sigma}} = \overline{\overline{\overline{\overline{C^e}}}} : \overline{\overline{E^e}} \qquad \textbf{Equation 3}$$

Where $\bar{\bar{\Sigma}}$, $\overline{\overline{\overline{\overline{C^e}}}}$, and $\overline{\overline{E^e}}$ are the second order macroscopic stress tensor, fourth order effective elastic stiffness tensor and the second order macroscopic elastic strain tensor. In equation 3, the second and fourth order tensors are symmetric and, therefore, they can be respectively reduced to 6 × 1 and 6 × 6 matrices using Voigt notations. The effective elastic fourth order tensor is characterized by 9 components and can be written in a matrix form, with respect to the principal material coordinate system. The 9 components of $\overline{\overline{\overline{\overline{C^e}}}}$ of the four joint patterns at different temperatures are reported in Table 1. It should be noted that for joint patterns O and H, some components of $\overline{\overline{\overline{\overline{C^e}}}}$ are functions of the macroscopic strains (E) in the respective direction. Because the homogenized Young's modulus $(\tilde{E})$ in the directions normal to bed (direction 1 or x) and head (direction 2 or y) joints and shear modulus ($\tilde{G}$, with respect to 12 plane or xy plane) increases with the gradual closure of joints (due to the increase of the contact area between the bricks with the gradual closure of joints). Therefore the effective normal and shear stiffness is increased. Examples of the identified homogenized Young's modulus $(\tilde{E})$ and shear modulus $(\tilde{G})$ of joint pattern O variations with the macroscopic normal (E_{ii}) and shear (E_{ij}) strains at different temperatures are presented in Figure 9.

The homogenized orthotropic viscoplastic strain rate second order tensor $\overline{\overline{\dot{E}vp}}$ of the four joint patterns can be described using the macroscopic form of the power creep law as follow [8], [18]:

$$\overline{\overline{\dot{E}vp}} = \frac{1}{2} A \left(\Sigma_{eq}\right)^{n-1} \overline{\overline{\overline{\overline{N}}}} : \bar{\bar{\Sigma}} \qquad \textbf{Equation 4}$$

Where *A* and *n* are materials parameters of the bricks, Σ_{eq} and $\overline{\overline{\overline{\overline{N}}}}$ are the macroscopic equivalent stress and a fourth order tensor with the same meaning of the localization tensor. The $\overline{\overline{\overline{\overline{N}}}}$ tensor accounts for the orthotropy and compressibility of the structure and enables using the creep parameters of the constitutive material (i.e. bridge between the micro and macro scales). The $\overline{\overline{\overline{\overline{N}}}}$ tensor is symmetric and can be represented by 6 × 6 matrix using the Voigt notations. The identified 9 components of $\overline{\overline{\overline{\overline{N}}}}$, by FE based nonlinear homogenization, of the four joint patterns at different temperatures are reported in Table 2. The negative values should be negative as, normally when a material is subjected to tensile creep in one direction, the viscoplastic strain rate in the loading direction is positive while being negative in the other 2 directions (elongation in one direction and decrease in thickness and depth in the other two directions). The identified homogenized elastic and viscoplastic parameters are used later in this work to predict the homogenized behaviour of masonry walls subjected to a wide range of thermomechanical loading conditions.

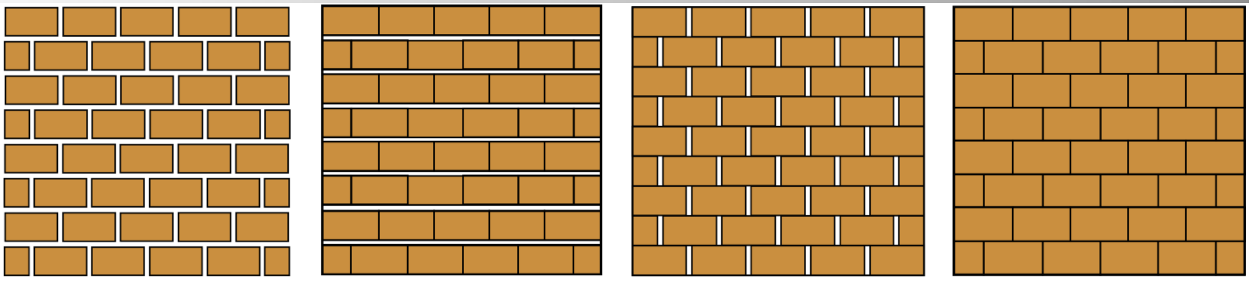

(a) (b) (c) (d)

Figure 8: Schematics of possible joint patterns of refractory masonry with dry joints (a) pattern O, (b) pattern H, (c) pattern B, and (d) pattern C.

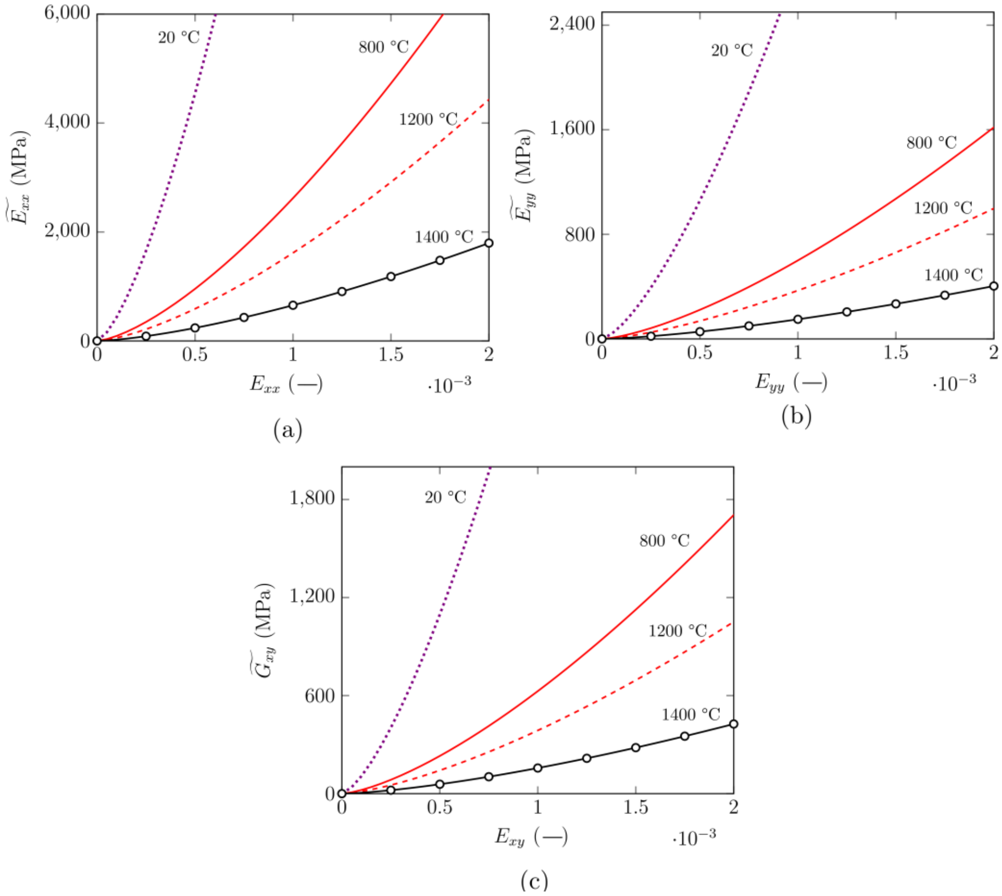

Figure 9: Examples of the identified homogenized (a, b) Young's modulus and (c) shear modulus variations with the macroscopic strains of joint pattern O at different temperatures.

Table 1: Effective elastic 4th order tensor of the four joint patterns of alumina spinel refractory masonry at different temperatures.

Pattern	$\overline{\overline{\overline{\overline{C}}}}^{e}\ (MPa)$																	
Temperature	20 °C						800 °C						1000 °C					
O	$f(E_{11})$	0	0	0	0	0	$f(E_{11})$	0	0	0	0	0	$f(E_{11})$	0	0	0	0	0
		$f(E_{22})$	0	0	0	0		$f(E_{22})$	0	0	0	0		$f(E_{22})$	0	0	0	0
			31666	0	0	0			6666	0	0	0			5444	0	0	0
				$f(E_{12})$	0	0				$f(E_{12})$	0	0				$f(E_{12})$	0	0
					11875	0					2500	0					2041	0
						11875						2500						2041
H	29687	0	5937	0	0	0	6666	0	1666	0	0	0	5444	0	1361	0	0	0
		$f(E_{22})$	0	0	0	0		$f(E_{22})$	0	0	0	0		$f(E_{22})$	0	0	0	0
			30299	0	0	0			6666	0	0	0			5444	0	0	0
				$f(E_{12})$	0	0				$f(E_{12})$	0	0				$f(E_{12})$	0	0
					11875	0					2500	0					2041	0
						11875						2500						2041
B	10394	2618	2602	0	0	0	2188	551	547	0	0	0	1787	450	447	0	0	0
		30307	6585	0	0	0		6380	1386	0	0	0		5210	1132	0	0	0
			30299	0	0	0			6378	0	0	0			5209	0	0	0
				8369	0	0				1762	0	0				1439	0	0
					11875	0					2500	0					2041	0
						11875						2500						2041
C	31666	7916	7916	0	0	0	6666	1666	1666	0	0	0	5444	1361	1361	0	0	0
		31666	7916	0	0	0		6666	1666	0	0	0		5444	1361	0	0	0
			31666	0	0	0			6666	0	0	0			5444	0	0	0
				11875	0	0				2500	0	0				2041	0	0
					11875	0					2500	0					2041	0
						11875						2500						2041

Pattern	$\overline{\overline{\overline{\overline{C}}}}^{e}\ (MPa)$											
Temperature	1200 °C						1400 °C					
O	$f(E_{11})$	0	0	0	0	0	$f(E_{11})$	0	0	0	0	0
		$f(E_{22})$	0	0	0	0		$f(E_{22})$	0	0	0	0
			4111	0	0	0			1666	0	0	0
				$f(E_{12})$	0	0				$f(E_{12})$	0	0
					1541	0					625	0
						1541						625
H	4111	0	1027	0	0	0	1666	0	416	0	0	0
		$f(E_{22})$	0	0	0	0		$f(E_{22})$	0	0	0	0
			4111	0	0	0			1666	0	0	0
				$f(E_{12})$	0	0				$f(E_{12})$	0	0
					1541	0					625	0
						1541						625
B	1349	339	337	0	0	0	547	137	136	0	0	0
		3934	854	0	0	0		1595	346	0	0	0
			3933	0	0	0			1594	0	0	0
				1086	0	0				440	0	0
					1541	0					625	0
						1541						625
C	4111	1027	1027	0	0	0	1666	416	416	0	0	0
		4111	1027	0	0	0		1666	416	0	0	0
			4111	0	0	0			1666	0	0	0
				1541	0	0				625	0	0
					1541	0					625	0
						1541						625

Table 2: Effective viscoplastic 4th order tensor of the four joint patterns of alumina spinel refractory masonry at different temperatures.

Pattern	$\overline{\overline{\overline{\overline{N}}}}$ $(--)$																	
Temperature	1300 °C						1400 °C						1500 °C					
O	2.22	-1.11	-1.11	0	0	0	2.16	-1.08	-1.08	0	0	0	2.25	-1.12	-1.12	0	0	0
		2.22	-1.11	0	0	0		2.16	-1.08	0	0	0		2.25	-1.12	0	0	0
			2.23	0	0	0			2.16	0	0	0			2.25	0	0	0
				9.33	0	0				8.29	0	0				9.71	0	0
					9.33	0					8.29	0					9.71	0
						9.33						8.29						9.71
H	2.22	-1.11	-1.11	0	0	0	2.16	-1.08	-1.08	0	0	0	2.25	-1.12	-1.12	0	0	0
		2.22	-1.11	0	0	0		2.16	-1.08	0	0	0		2.25	-1.12	0	0	0
			2.23	0	0	0			2.16	0	0	0			2.25	0	0	0
				9.33	0	0				8.29	0	0				9.71	0	0
					9.33	0					8.29	0					9.71	0
						9.33						8.29						9.71
B	15.07	-1.59	-1.03	0	0	0	11.81	-1.32	-1.08	0	0	0	11.36	-1.50	-1.12	0	0	0
		2.22	-1.11	0	0	0		2.16	-1.08	0	0	0		2.25	-1.12	0	0	0
			2.23	0	0	0			2.16	0	0	0			2.25	0	0	0
				17.06	0	0				12.52	0	0				13.34	0	0
					9.33	0					8.29	0					9.71	0
						9.33						8.29						9.71
C	2.22	-1.11	-1.11	0	0	0	2.16	-1.08	-1.08	0	0	0	2.25	-1.12	-1.12	0	0	0
		2.22	-1.11	0	0	0		2.16	-1.08	0	0	0		2.25	-1.12	0	0	0
			2.23	0	0	0			2.16	0	0	0			2.25	0	0	0
				9.33	0	0				8.29	0	0				9.71	0	0
					9.33	0					8.29	0					9.71	0
						9.33						8.29						9.71

4 Wallets under vertical uniaxial setup

4.1 Brief description of the experimental setup

The experimental tests were carried out at the Laboratory of Testing Materials of the University of Coimbra, in Portugal. A general overview of the test setup can be seen in Figure 10. The test set-up consists of one reaction frame composed by two HEB500 columns and two overlapping HEB600 beams (4500 mm span). The hydraulic jack had the capacity of 3 MN and the load cell used to measure the applied load had the capacity of 5 MN. For the experiments performed at high temperatures one modular electric furnace (45 kVA) was used to heat the specimens. Additional details regarding the experimental setup, the specimens and the acquisition systems can be seen in *Deliverable D4.3*. When referring to the numerical results, the name for every test series was kept the same for ease of understanding and following both this deliverable and *Deliverable D4.3*.

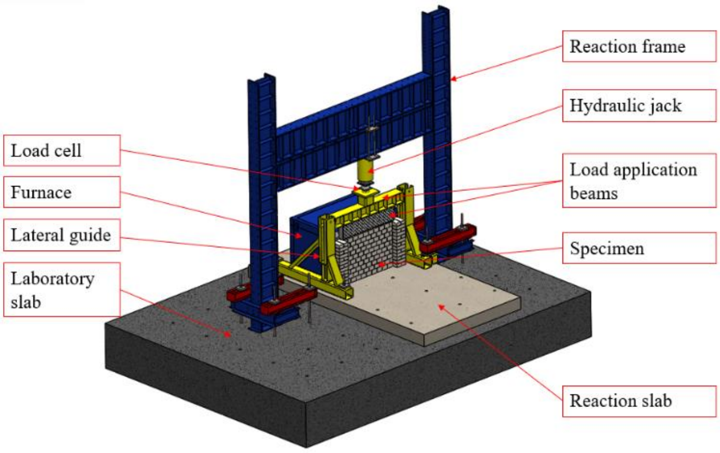

Figure 10: Experimental setup used to perform uniaxial compression tests of alumina spinel refractory masonry walls.

From the experimental programme developed in the scope of ATHOR, which intended to assess the loadbearing capacity of the walls at high temperatures in service conditions, two uniaxial tests were chosen to be simulated here. The first one is series S01.AT.LBC, a uniaxial compressive test carried at room temperature, which aimed to assess the loadbearing capacity of the wall. The other test chosen here, series S03.HT.LL8, is carried out at high temperatures and aimed to assess the thermomechanical behaviour of the masonry under a constant load level. Firstly, a mechanical load of 8 MPa was applied to the specimen, then the wall was heated up according to ISO 834-1 [20]. The pictures of the experimental high temperature set-up are presented in Figure 11. The walls geometry is presented in Figure 12.

a) b)

c)

Figure 11: Test set-up at high temperatures:
a) Front view; b) Detail of the furnace and reaction slab and c) Detail of bottom insulation.

European Commission
Horizon 2020
European Union funding
for Research & Innovation

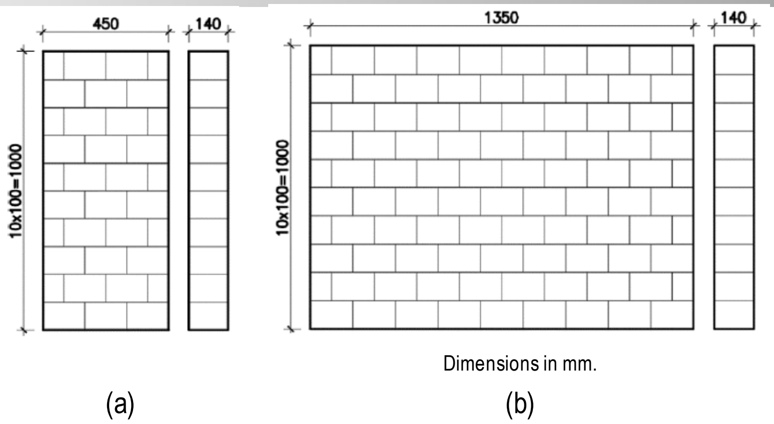

Figure 12: Specimen's dimensions, (a) Series S01.AT.LBC; (b) Series S03.HT.LL8 [21].

4.2 S01.AT.LBC: uniaxial compression up to failure at room temperature

In this test series, three refractory masonry walls with dimensions 450×1000×140 mm^3 (Figure 12a) were tested up to failure. The objective of this test series was to assess the loadbearing capacity of the refractory masonry walls. The test procedure in series S01.AT.LBC had the following steps: i) the masonry specimens were built in the testing system; ii) the loading beams were placed on the top of the specimens using a crane; iii) the instrumentation was installed; iv) the loadbearing capacity test was performed under displacement control at a rate of 0.01 mm/s up to failure of the specimen.

The FE models of the wall are presented in Figure 13. The FE model for micro-model approach (Figure 13a) was developed using DIANA software. The masonry walls geometry was discretized using an 8-node isoparametric solid brick element. The final mesh was generated automatically by the DIANA software with 20 mm × 20 mm × 20 mm elements. For the mechanical and thermal analysis, HX24L elements were used. These HX24L elements are three-dimensional continuum isoparametric solid brick elements, based on linear interpolation, Gauss integration, and orthogonal hourglass control.

The homogenised FE model (Figure 13b) was developed using the Abaqus software and the wall was meshed with 3D hexahedron elements. The top loading beam and the reaction slab of the test setup were replaced with rigid plates. The wall (bricks and joints) is represented by a homogeneous material whose mechanical properties depend on the state of bed and head joints (open or closed). The interactions between the contact surfaces of reaction slab and the wall and between the loading beam and the wall were modelled using friction contact with a coefficient of friction of 0.5. The boundary conditions of the two rigid plates are given in Figure 13b. The sides of the wall were free during load application step. The gravity effects (weight of the bricks) were considered in the FE model.

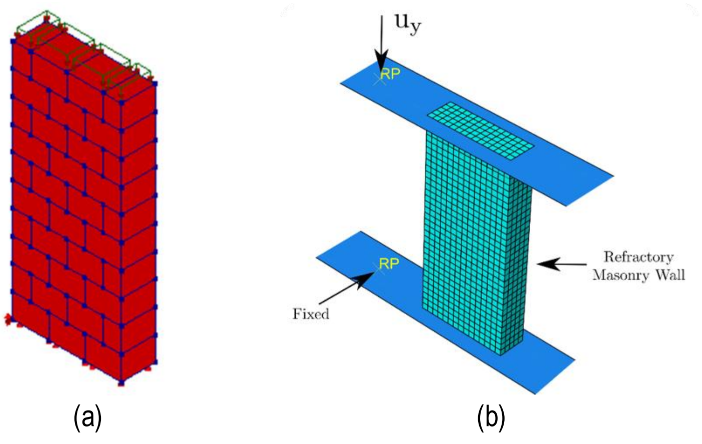

Figure 13: Test series S01.AT.LBC FE, model of a masonry wall subjected to uniaxial compression load in the direction normal to bed joints, a) Micro-model and b) Macro-model.

4.2.1 Results from the Micro-model

The vertical displacement fields predicted by the numerical model (in the direction normal to bed joints - loading direction) on the front surface of the wall at 33 %, 66 % and 100 % of maximum load level is presented in Figure 14. The comparison of the numerical and experimental stress-strain curves for series S01.AT.LBC is shown in Figure 15. The curve from the finite element analysis fits closely with the experimental data. Three stages can be observed in the experimental and numerical curves: (i) joint closure; (ii) linear behaviour; (iii) damageable plastic behaviour and failure. Finally, the developed finite element model shows adequacy to the representation of the problem.

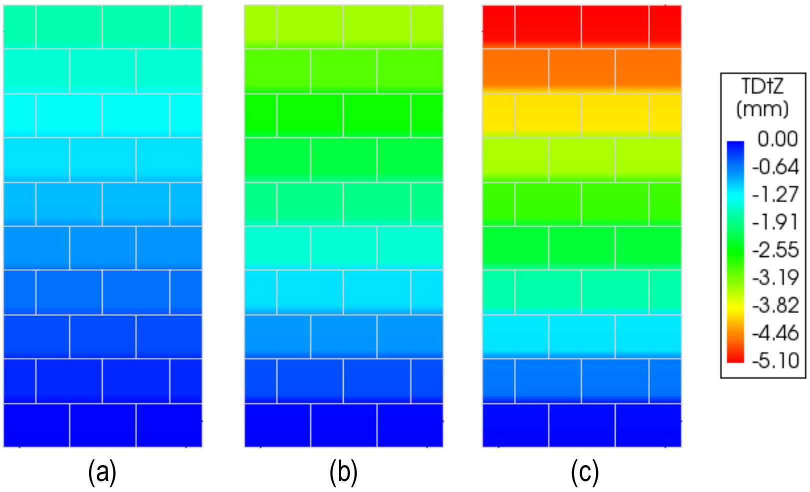

Figure 14: Test series S01.AT.LBC, vertical displacement fields in masonry wall subjected to uniaxial compression load in the vertical direction at (a) 33 %, (b) 66 % and (c) 100 % of maximum load level.

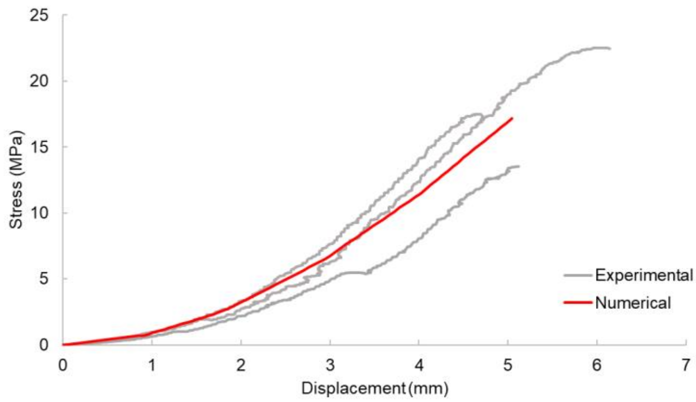

Figure 15: Validation of the numerical model - test series S01.AT.LBC.

4.2.2 Results from Macro-model

The vertical displacement fields predicted by the numerical model (in the direction normal to bed joints - loading direction) on the front surface of the wall, at 33 %, 66 % and 100 % of maximum load level, are presented in Figure 16. Comparisons between the experimental and numerical reaction forces variations with the displacement are shown in Figure 17. The displacements of the experimental tests were determined from the DIC analysis. Good agreements between the experimental and numerical results can be observed. It can be noticed that the present multi scale numerical model can reproduce, with reasonable accuracy, the nonlinear mechanical response of the wall. The resulting force displacement diagram of the wall is nonlinear. The numerical model is able to predict the displacement stiffening behaviour of the wall caused by the progressive closure of joints and the gradual increase in the contact area with the increase of the applied load (increase of effective stiffness and effective tangent Young's modulus of the wall with the increase of the applied load).

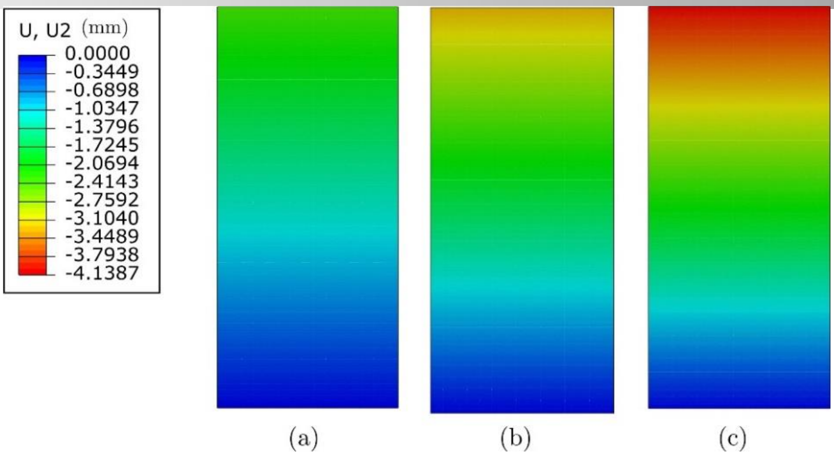

Figure 16: Test series S01.AT.LBC, vertical displacement fields in masonry wall subjected to uniaxial compression load in the direction normal to bed joints (vertical direction in this image) at (a) 33 %, (b) 66 % and (c) 100 % of maximum load level.

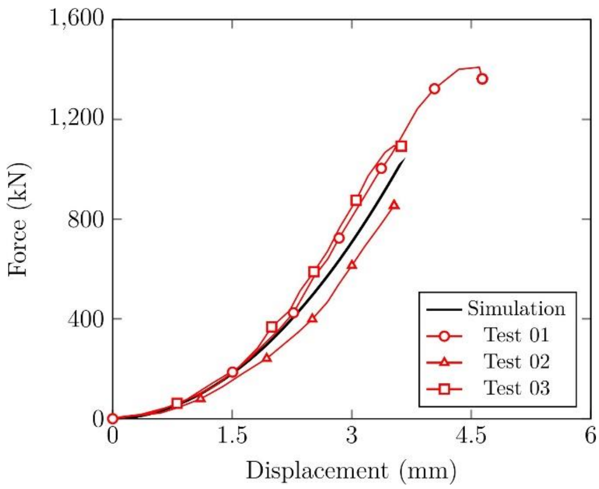

Figure 17: Test series S01.AT.LBC, displacement, in the direction normal to bed joints, versus vertical reaction force in alumina spinel masonry wall subjected to uniaxial compression load, up to failure, at room temperature, experimental and numerical results.

4.3 S03.HT.LL8: uniaxial compression at high temperature

In this test series, three refractory masonry walls with dimensions 1350×1000×140 mm^3 (Figure 12(b)) were tested. Series S03.HT.LL8 was tested at high temperatures. Steps i, ii and iii of the test procedures were similar to those presented for series S01.AT.LBC. Then: iv) the specimen was loaded under displacement control at a rate of 0.01 mm/s up to 8 MPa at ambient temperature, v) the control procedure was changed to load control and set to keep the current load; vi) the furnace was turned on and then programmed to heat according to the temperature evolution proposed by the standard fire curve ISO 834-1 [20]; vii) the wall was monitored for five hours: the temperatures, applied load, in-plane and out-of-plane displacements were recorded. The specimens were not tested up to the failure due to limitations on the maximum operating time of the furnace. However, due to the high thermal capacitance of the specimen, the furnace was not able to follow the programmed heating curve [21]. The effective temperature measured in the furnace during the three tests is shown in the dashed lines S03-01, S03-02 and S03-03 presented in Figure 18. The thermal load applied to the furnace - the standard fire curve ISO 834-1 [20], is presented by the continuous line in black.

In the developed finite element models, two analyses were performed consecutively for each variation of increment of external conditions: (i) first, heat transfer analysis, and (ii) second, mechanical analysis. The objective of the heat transfer analysis is to determine the temperature fields in the wall throughout the test. The results of this analysis are then used as the input for the mechanical analysis. Which aims to simulate the structural behaviour of the dry-stacked masonry.

The heat transfer model considers the radiative ($q_{r,i}$) and convective ($q_{c,i}$) heat exchange between the furnace and the hot face (HF) of the wall, conductive (q_{con}) heat transfer through the wall thickness, convective ($q_{c,o}$) and radiative ($q_{r,o}$) heat exchange between the cold face (CF) and the ambient. Figure 19 shows the thermal resistance diagram used to simulate these phenomena. The heat transfer model uses theoretical equations to determine the radiation, convection, and conduction heat transfer.

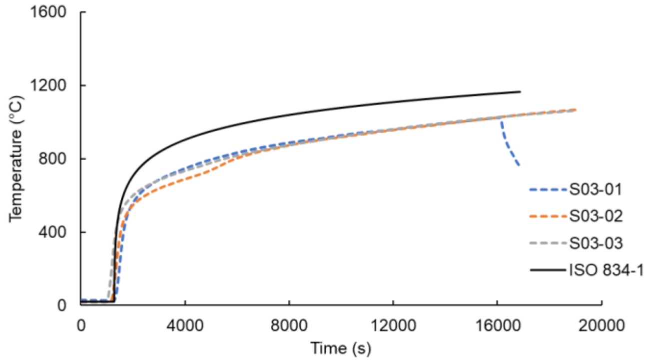

Figure 18: Thermal load programmed into the furnace (in black) and temperature values measured inside the furnace (dashed lines).

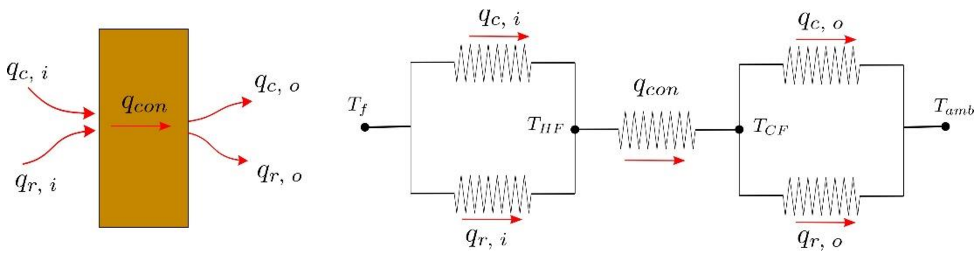

Figure 19: Test series S03.HT.LL8, schematic of the thermal model of the wall and the thermal resistance circuit equivalence.

The temperature distribution of the wall varies with time (t) and can be obtained by solving the transient form of energy equation given by [22]:

$$\rho C_p \frac{\partial T}{\partial t} - \mathrm{div}\ (k\overrightarrow{\mathrm{grad}}\,(T)) = 0 \qquad \textbf{Equation 5}$$

Where ρ, k, T and C_p are the density, thermal conductivity, temperature and specific heat, respectively. Before heating, the initial temperature (T_i) of wall is assumed to be the same as ambient temperature. Under this assumption, the initial boundary conditions can be expressed as [22]:

$$T(R, \theta, Z, t = 0) = T_i = 20°\mathrm{C} \qquad \textbf{Equation 6}$$

The convective heat flux exchange ($q_{c,i}$) between the furnace (f) and the HF of the wall is written as [22]:

$$q_{c,i} = h_i\big(T_f - T_{HF}(x, y, z, t)\big) \qquad \textbf{Equation 7}$$

$$\frac{\partial T_{hf}}{\partial \vec{n}} = h_i\big(T_f - T_{HF}(x, y, z, t)\big)\vec{\mathrm{n}} \qquad \textbf{Equation 8}$$

Where h_i is the convective heat transfer coefficient and $\vec{\mathrm{n}}$ is the outward normal to the surface. The radiative heat flux ($q_{r,i}$) exchange between the furnace and the HF is expressed as:

$$q_{r,i} = \epsilon S\big(T_f^4 - T_{HF}^4(x, y, z, t)\big) \qquad \textbf{Equation 9}$$

Where ϵ and S are the emissivity of the wall and Stefan–Boltzmann constant, respectively. The convective ($q_{c,o}$) and radiative ($q_{r,o}$) heat losses from the CF of the wall to the ambient (amb) are expressed as [22]:

$$q_{out} = q_{c,o} + q_{r,o} = h_o(T_{CF}(x, y, z, t) - T_{amb}) + \epsilon S\big(T_{CF}^4(x, y, z, t) - T_{amb}^4\big) \qquad \textbf{Equation 10}$$

Where h_o is the convective heat transfer coefficient between the CF of the wall and the ambient.

European Commission | Horizon 2020 European Union funding for Research & Innovation

4.3.1 Results from Micro-model

The heat transfer and thermomechanical FE models of the wall were developed using the DIANA FEA software. In the heat transfer analysis, the model was fed with the thermal properties (taken as temperature-dependent) and density of the alumina spinel brick. The initial temperature of the system and the gas temperature of the furnace throughout the test were input in the analysis. The analysis accounts for convection, conduction, and radiation heat transfer. The interfaces between the bricks have been considered with the same thermal conductivity as the material. At the exposed and non-exposed face, the radiation was represented as surface radiation and the convection was represented as a surface film condition. Due to the thermal insulation material used in the experimental system, adiabatic surfaces were considered between the wall and the reaction slab, the lateral masonry columns, and the loading beam. Consequently, all heat losses took place on the non-exposed face. The convection coefficient was taken as 25 W/m^2°C in the exposed face [23] and taken as 10 W/m^2°C in the cold face. The resultant emissivity of the system was taken as 0.18. This value relates to the system formed by the bricks and the furnace itself, and since the efficiency of the heating elements and their disposition were not ideal, the overall value of emissivity of the system is low. Different locations of the exposed wall's surface were assumed to be, in each instant, at a constant temperature. This was confirmed by thermocouples installed in the test specimens. The temperatures in the first course of the bricks (bottom of the wall), measured by the thermocouples, were lower than the average temperatures of the wall (Refer to *Deliverable D4.3* for more in-depth discussion regarding the experimental results). This was caused, in part, by the furnace's internal arrangement of the resistances, making this area less exposed to thermal radiation (Figure 11(b)), due to heat losses through the reaction slab (Figure 11(b)) and the bottom insulation (Figure 11(c)), and due to the air convection currents inside the furnace. In general, a relatively homogeneous temperature distribution was found in the wall within a range of ±15 %. Therefore, the temperature was considered to vary through the height of the wall within 15% of the measured values. The minimum temperature was applied to the bottom and the maximum to the top of the wall.

To execute the mechanical analysis, the brick's Young's modulus, thermal elongation coefficient, density, compressive strength, tensile strength, and fracture energy, with temperature-dependent values were fed to the model. The temperature fields generated in the heat transfer analysis were used by the software to calculate the thermal strains in each element and the variation of the mechanical properties. The mechanical load was applied uniformly on the top surface of the wall. Suitable boundary conditions were applied at the bottom surface of the masonry, to represent the boundary conditions provided by the experimental setup.

The temperature evolutions are presented in Figure 20. In Figure 20(a), the hot face (HF) and cold face (CF) results are presented. It shows in grey, the maximum and minimum curves measured for each face, in black the results from numerical analysis. The furnace load is shown in red.The temperature distribution at the end of the heating step is presented in Figure 20(b). The temperature curves of the FEA analysis fit in-between the measured temperature limits. This agreement is important to ensure the adequacy of the developed finite element model for the heat transfer analysis, and consequently to correctly input the thermal load at the mechanical analysis.

The comparison of the in-plane displacements, on top of the masonry, obtained experimentally and numerically are presented in Figure 21. At the beginning of the test, from 0 to 1200 s, as the pre-compression stress of 8 MPa was applied, negative displacements were observed because of the joint closure and bricks deformation. The furnace was then turned on and the temperatures at the hot face started to increase. With the beginning of the heating procedure, the effects of the thermal elongation started to increase, and the wall presented a positive strain rate. During the period between 1200 s to 2700 s, there are some differences among the numerical and experimental in-plane displacements, that may have been caused by rotation of the load application beam in its longitudinal axis, induced by the beginning of the thermal bowing of the wall. Nevertheless, the developed model can represent all stages of the test, including the effects of the thermal elongation on the masonry walls.

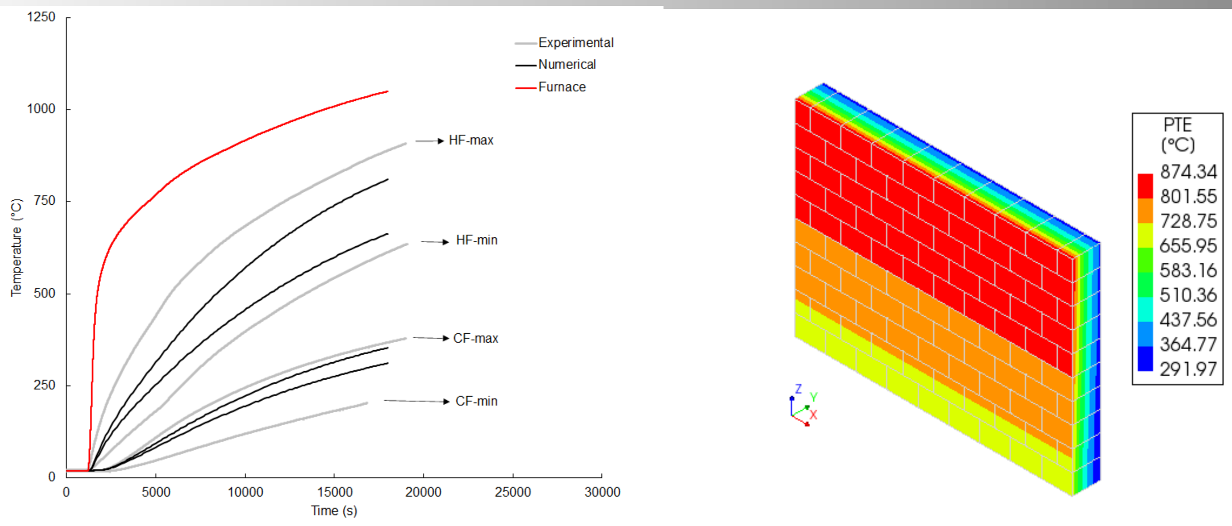

(a) (b)

Figure 20: Validation of the numerical model - test series S03.HT.LL8 temperature evolution: (a) Temperature vs. time evolution on the hot and cold face, (b) Temperature distribution at the end of the heating step.

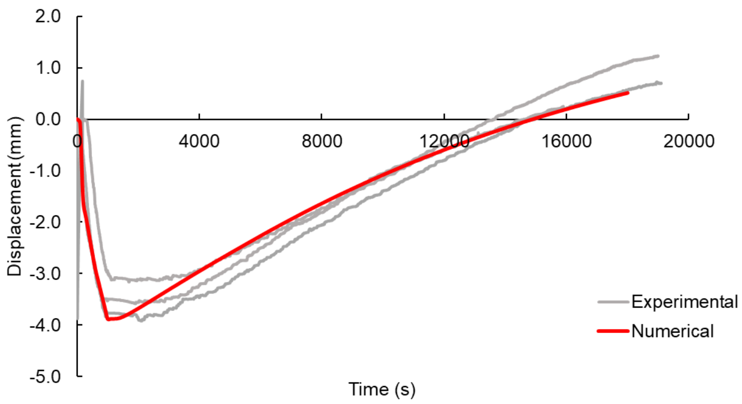

Figure 21: Validation of the numerical model in-plane displacements - test series S03.HT.LL8.

4.3.2 Results from Macro-model

The heat transfer and thermomechanical FE models of the wall were developed using the Abaqus software. The physical model of the wall is similar to that of series S01.AT.LBC with only one difference, which is the width of the wall (1350 mm in the case of series S03.HT.LL8).

Regarding the heat transfer analysis, the value of h_o was equal to 5 W/m^2.K (natural convection from a flat surface) and the emissivity of alumina spinel was taken as 0.8. The value of h_i changes with temperature of the HF of the wall (i.e. solution dependent). The experimental and numerical time variations of the temperature of the HF and CF at different locations of the wall during load application and heating steps are shown in Figure 22(a). The shaded areas in the figure present the readings of the thermocouples. Good agreements between the experimental and numerical results can be observed. The temperature distribution at the end of the heating step is presented in Figure 22(b). During load application step (first 1800 seconds), the temperature was equal to room temperature. Then, during the heating step, heat is transferred by convection and radiation mechanisms from the furnace to the HF of the wall. As a result, the temperature of the HF increases gradually from room temperature to around 880 °C. The high temperature gradients through the thickness of the wall are caused by the low thermal conductivity, high heat thermal capacity of alumina spinel and high heat losses from the CF to the ambient.

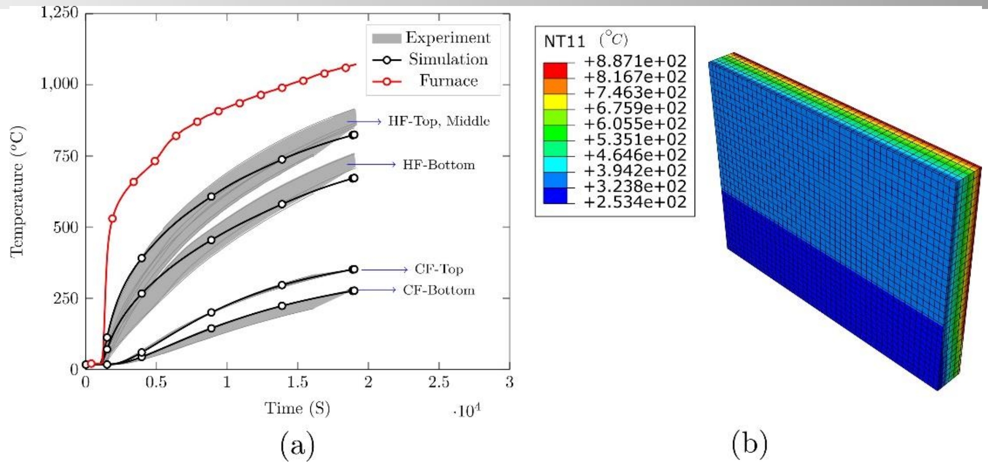

Figure 22: Test series S03.HT.LL8, (a) time variations of the hot face and cold face temperatures, experimental and numerical results, (b) Temperature distribution at the end of the heating step.

Regarding the thermomechanical analysis, the wall has been replaced by a homogeneous material whose mechanical properties vary with the gradual closure and reopening of joints. The loading beam and the reaction slab were replaced by rigid plates. The frictional interactions between the contact surfaces of the reaction slab and the wall and between the loading beam and the wall were considered (coefficient of friction 0.5). The applied load to the top loading beam is a compressive stress of 8 MPa. The same experimental amplitude was used for load application and load holding steps. The sides of the wall were free to move during load application and holding. The temperature distributions obtained from the heat transfer analysis were employed as a thermal load in the transient thermomechanical analysis.

The experimental and numerical time variations of the displacement in the direction normal to bed joints are given in Figure 23. Good agreements between the experimental and numerical results can be observed. From the figure, one can observe that in the first 1800 seconds, an average negative displacement of around -3.5 mm was measured by the LVDTs and predicted by the numerical model due to uniaxial compression load application (8 MPa). Then, when the furnace was turned on and with the increase of the temperature, the wall started to expand gradually and a steady increase in the displacement, in the opposite direction, was recorded. At around 16000 seconds, the thermal expansion effects of the wall over passed the impact of mechanical load application and a positive displacement was recorded by the LVDTs and predicted by the present model.

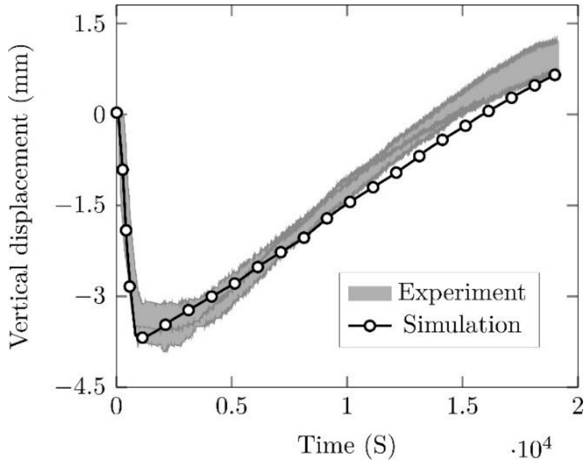

Figure 23: Test series S03.HT.LL8, experimental and numerical time variations of the vertical displacement.

5 Wallets in horizontal biaxial setup

5.1 Brief description of the experimental setup

These experimental tests were carried out at the Technology Centre Leoben (TCL) of RHI-Magnesita, in Austria. This test setup has been used before (Prietl, 2006) and was improved for this experimental campaign. The schematic overview of the test setup is presented in Figure 24. The test setup consisted of a monolithic reaction frame in which the hydraulic jacks, LVDTs and heating system were connected. Two orthogonal hydraulic jacks with the capacity of 1000 kN were used, with a Rexroth controller unit. The applied forces were measured by two pressure gauges per cylinder. A 48-channel data acquisition system was used to record the data from the experiments. Additional details regarding the experimental setup, the specimens and the acquisition systems can be seen in *Deliverable D4.3*. When referring to the numerical results, the same name for every test series was kept the same for consistency and ease of understanding between this deliverable and *Deliverable D4.3*.

Thirteen tests of alumina spinel refractory masonry walls were performed. Six of them were performed at room temperature and the remaining eight tests were carried out at high temperature. The test series names, loading conditions in directions perpendicular to the surfaces of bed and head joints and testing temperature are given in Table 3. For all tests, the dimensions of the walls are 1125×1100×140 mm^3.

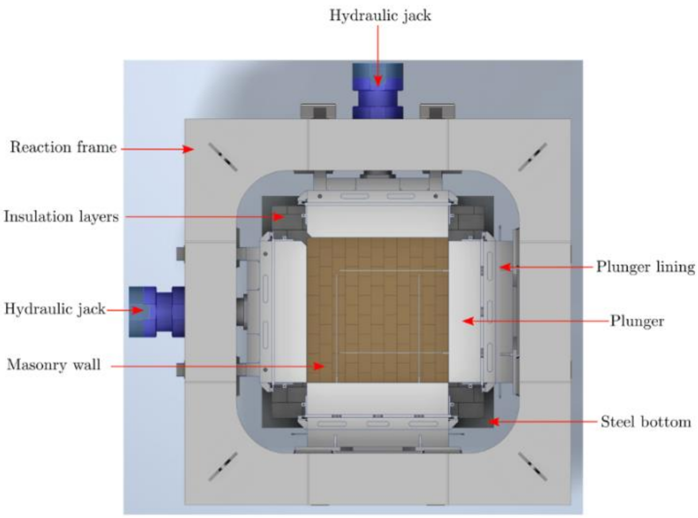

Figure 24: Top view of the biaxial compression test field.

Table 3: Summary of the biaxial compression tests of refractory masonry walls performed at room and high temperatures.

Series	Specimen	Maximum load		Temperature
		Bed	**Head**	
S06.AT. LBJ	S06.AT. LBJ.01	6 MPa	Constrained	Room temperature
	S06.AT. LBJ.02			
S07.AT. LHJ	S07.AT. LHJ.01	Constrained	6 MPa	
	S07.AT. LHJ.02			
S08.AT.LBI	S08.AT.LBI.01	6 MPa	6 MPa	
	S08.AT.LBI.02			
S09.HT.CBJ	Preliminary test	6 MPa	Constrained	High temperature
	S09.HT.CBJ.01	4 MPa		
	S09.HT.CBJ.02			
S10.HT.CBI	S10.HT.CBI.01	4 MPa	4 MPa	
	S10.HT.CBI.02			
S11.HT.RBI	S11.HT.RBI.01	4 - 6 MPa	4 - 6 MPa	
	S11.HT.RBI.02			

5.2 S06.AT. LBJ: uniaxial loading and unloading - normal to bed joints at room temperature

In this test series, two refractory masonry walls with dimensions 1100×1125×140 mm^3 were tested at room temperature. A uniaxial compression load/unload (up to 6 MPa) was applied in the direction normal to the bed joints and the direction normal to the head joints was constrained by the plungers. The FE models of the wall are shown in Figure 25. The x-direction (1125 mm) is the direction normal to the head joints while, the y-direction (1100 mm) is normal to the bed joints. The FE models were developed using the Abaqus software and the wall was meshed with 3D hexahedron elements (C3D8T). The four ceramic plates, as well as the top insulation layer (ground) of the test setup have been modelled as rigid plates. The units (refractory bricks) and dry joints were modelled separately in the micro-model approach (Figure 25a). The wall (bricks and joints) was replaced by a homogeneous material for macro model approach (Figure 25b) whose mechanical properties depend on the state of bed and head joints (open or closed). The boundary conditions of two fixed rigid plates, the moving rigid plate normal to head joints (x-direction in Figure 25) and the ground are fully fixed. For both modelling approaches, frictional interactions between the contact surfaces of the wall and the fixed, moving rigid plates and the ground were considered (coefficient of friction of 0.5).

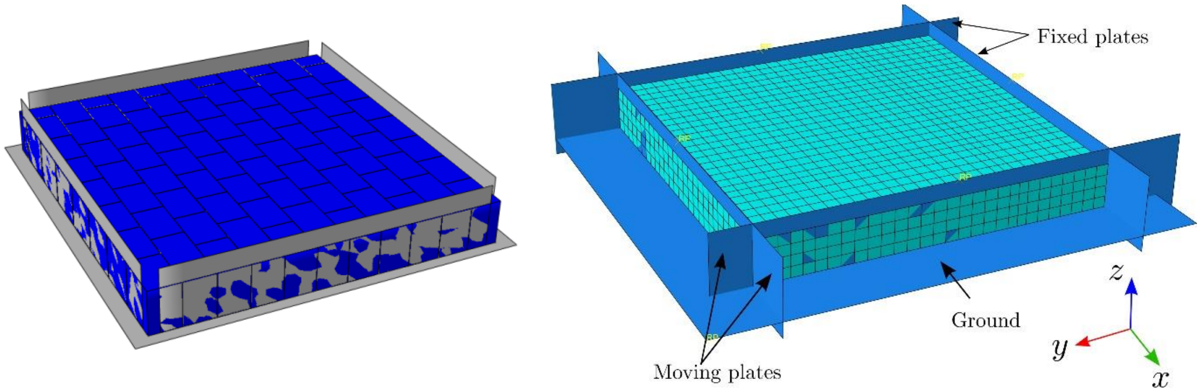

(a) (b)

Figure 25: Test series S06.AT.LBJ, FE model of a masonry wall subjected to uniaxial compression loading/unloading in the direction normal to bed joints, a) Micro-model; b) macro-model.

For this and all the subsequent simulations with micro-model approach (Figure 25a), the brick is assumed as elastic due to the low level of forces applied during the experiment. The thermomechanical properties used for the refractory brick are presented in Figure 1. The dry joints between the brick units are modelled as surface-to-surface contacts in Abaqus. For the normal behaviour of the joints, a tabular form of stress-joint closure values was used. Different joint overclosure diagrams are shown in Figure 26 [21]. For this simulation and all the subsequent analyses, the values are derived from the red profile (Wallet 1350×140). However, this relation was used only for the initial loading. The values for unloading and reloading were derived from the experimental data used to compare this simulation. For the tangential behaviour of the dry joint, the friction values were used. These values were temperature depended [21] as shown in Table 4.

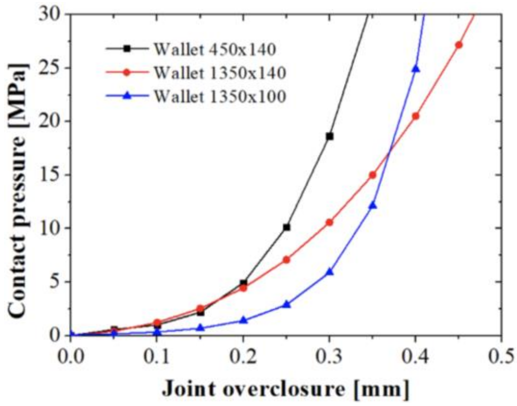

Figure 26: Contact pressure-overclosure relations used for different walls dimensions [21].

Table 4: Friction coefficient values for dry joints at different temperatures [21].

Temperature (°C)	Friction coefficient (-)
20	0.598
300	0.498
600	0.510
900	0.530

For the numerical simulation performed at high temperature, Norton-Bailey creep parameters were used alongside the thermal and elastic properties of the refractory bricks. The creep parameters are temperature dependent as shown in Table 5.

Table 5: Norton-Bailey creep law parameters corresponding to different temperatures [1].

Temperature (°C)	K (MPa^{-n}s^{-1})	n (-)	a (-)
1300	1.49E-11	1.0944	-0.7218
1400	3.29E-11		
1500	4.87E-11		

5.2.1 Results from Micro-model

Comparisons between the experimental and numerical force - displacement diagrams of a masonry wall subjected to uniaxial compression loading/unloading in the direction normal to bed joints are presented in Figure 27. It can be observed that considered material properties and dry joint behaviour from previous tests obtains a similar behaviour of the experiment. During initial loading period, observed stiffness is lower due to dry joints. This stiffness increases, with gradual increase in load, due to crushing of surface asperities present in dry joints. After the first peak loading (6 MPa), the unloading and reloading behaviour observed in the numerical simulation, matches the trend of experimental results. After first loading, the wall does not recover to its initial position due to closing of dry joints. Figure 28a presents the displacement field obtained from the simulation at the first peak. It can be observed that almost all the displacement occurs due to closing of dry joints and bricks behave as a rigid units for this low level of applied stress. Figure 28b shows the distribution of von Mises stresses at the first peak load. From the figure it is possible to observe that the stress is distributed uniformly at 6 MPa in the bricks except at areas near head joints. This is due to presence of dry joints.

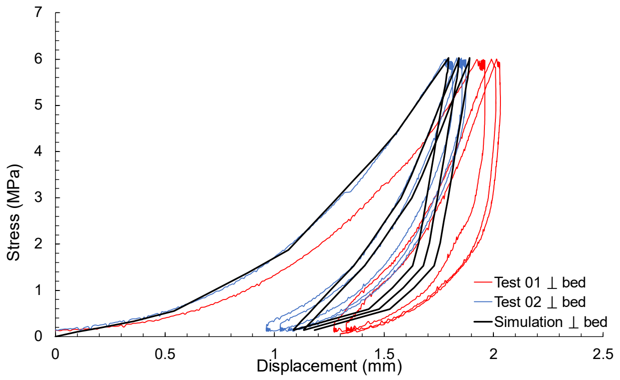

Figure 27: Test series S06.AT. LBJ, comparisons between experimental and numerical force - displacement diagrams of a masonry wall subjected to uniaxial compression loading/unloading in the direction normal to bed joints.

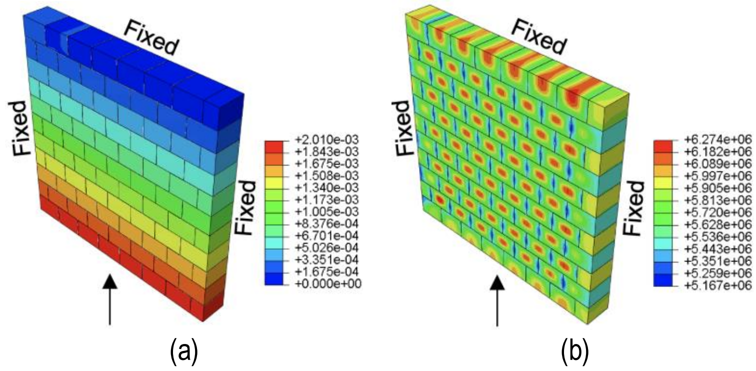

Figure 28: Test series S06.AT. LBJ, a) displacement distribution (mm) and b) Von Mises stress distribution (Pa).

5.2.2 Results from Macro-model

Comparisons between the experimental and numerical force - displacement diagrams of a masonry wall subjected to uniaxial compression loading/unloading in the direction normal to bed joints are presented in Figure 29. The bounds of the shaded area represent the results of the two experiments. The present numerical model can reproduce with reasonable accuracy the displacement stiffening mechanical behaviour of the wall. The reaction force increases with the increase in the displacement due to the gradual closure of the joints and the increase in effective stiffness with the gradual closure of joints. The displacement fields in the direction normal to bed joints at maximum load level and after load removal are given in Figure 30. The arrow indicates the location of the moving plunger (in the y-direction) and the lines denote the positions of the fixed plunger (in the x-direction) and the two fixed rigid plates. After unloading, the wall did not recover to the initial configuration and there was permanent deformation caused by the closure of joints, the deformation and the crushing of the asperities present at the contact surfaces of bed joints.

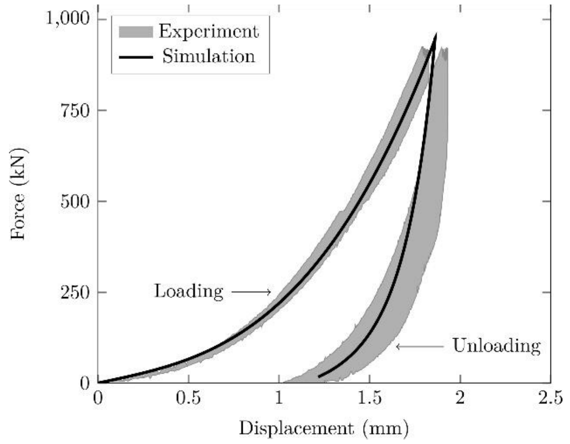

Figure 29: Test series S06.AT.LBJ, comparisons between experimental and numerical force - displacement diagrams of a masonry wall subjected to uniaxial compression loading/unloading in the direction normal to bed joints.

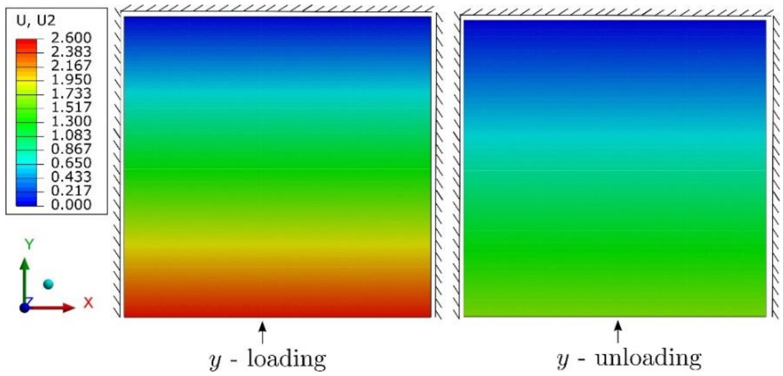

Figure 30: Test series S06.AT.LBJ: displacement fields (in mm), in the direction normal to bed joints, of a masonry wall subjected to uniaxial compression loading/unloading in the direction normal to bed joints (y direction) at maximum load level (left) and after unloading (right).

5.3 S07.AT.LHJ: uniaxial loading and unloading - normal to head joints at room temperature

Regarding test series S07.AT.LHJ, two refractory masonry walls with dimensions 1100×1125×140 mm^3 were tested at room temperature. The main difference between S07.AT.LHJ and S06.AT.LBJ is that the uniaxial compression loading (6 MPa) and unloading was applied to the direction normal to head joints while the other direction (normal to bed joints) was constrained by the ceramic plungers. The FE models of the wall are the same as that presented in Figure 25. The main difference between the two FE models is the boundary conditions of the two moving plungers. The frictional interactions between the contact surfaces of the wall, the plungers and the ground were considered in the FE model. The boundary conditions of two fixed rigid plates, the moving rigid plate normal to bed joints (y direction in Figure 25) and the ground are fully fixed.

5.3.1 Results from Micro-model

Experimental and numerical force - displacement diagrams of a wall subjected to uniaxial compression loading/unloading in the direction normal to head joints are shown in Figure 31. The numerical model was able to predict the mechanical behaviour of the wall with good accuracy. As compared to S06.AT. LBJ, the value of the displacement at maximum load level is smaller. This can be attributed to the number of head joints in the wall is less than the number of bed joints. This leads to higher stiffness (and, therefore, less deformation at the same load level) in the direction normal to head joints as compared to the direction normal to bed joints. Figure 32a makes the same observation as in Series S06.AT. LBJ where bricks behave almost as rigid units for low level of stress. Figure 32b shows the distribution of von Mises stresses at the first peak load. From the figure, it is possible to observe that the stress is distributed uniformly at 6 MPa in the bricks except at areas near the support for the head joint (right side of the figure). This high concentration can be explained due to high friction in the bed joints near support due to restricted movement and the dimension mismatch of the bricks near the support. The bricks are laid alternatively, in one layer there is full brick near the support and in the second layer there is half brick. The difference in shear displacement between those two bricks at the bed joint creates an alternative distribution of the stress in the bricks near the support. As a result, full bricks near support experience high stress (7 MPa) and half bricks experience stress around 4.5 MPa.

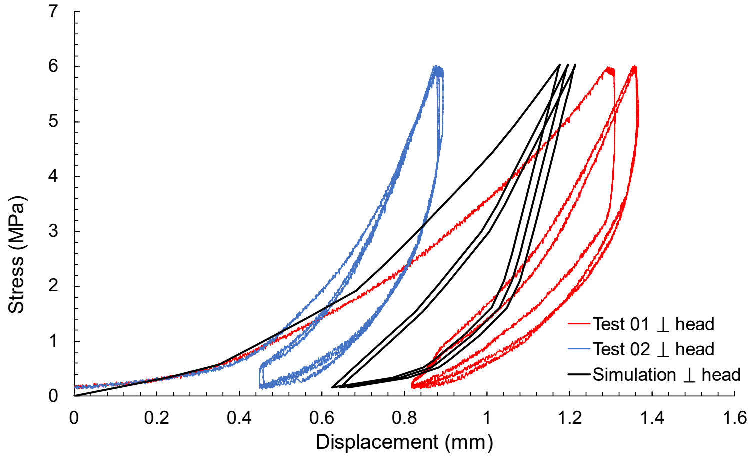

Figure 31: Test series S07.AT. LHJ, comparisons between experimental and numerical force - displacement diagrams of a masonry wall subjected to uniaxial compression loading/unloading in the direction normal to head joints.

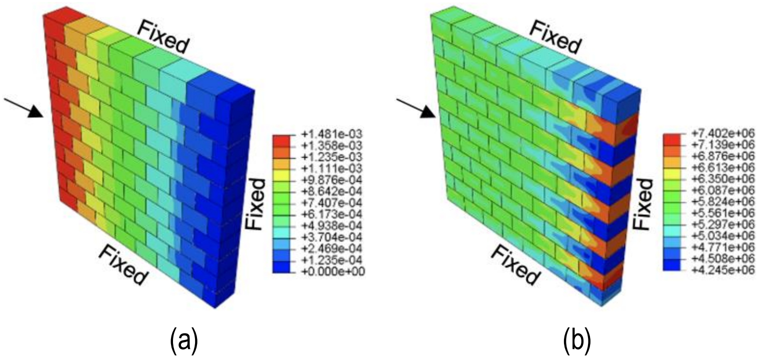

Figure 32: Test series S07.AT. LHJ, a) displacement distribution (mm) and b) Von Mises stress distribution (Pa).

5.3.2 Results from Macro-model

Figure 33 shows a comparison between experimental and numerical force - displacement diagrams of a wall subjected to uniaxial compression loading/unloading in the direction normal to head joints. The numerical model was able to predict the mechanical behaviour of the wall with good accuracy. As compared to S06.AT.LBJ, the value of the displacement at maximum load level is smaller. This can be attributed to that the number of head joints in the wall is less than the number of bed joints. This leads to higher stiffness (and, therefore, less deformation at the same load level) in the direction normal to the head joints as compared to the direction normal to the bed joints. Figure 34 shows the displacement fields in the direction normal to the head joints at the maximum load level and after unloading. The arrow indicates the location of the moving plunger (in the x-direction) and the lines denote the positions of the fixed plunger (in the y-direction) and the two fixed rigid plates. The wall did not go back to the initial configuration and there was permanent deformation caused by gradual closure of joints, the deformation and the crushing of the asperities present at the contact surfaces of head joints.

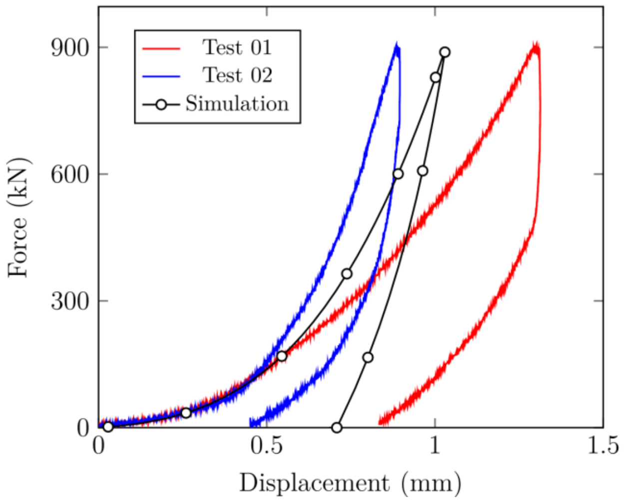

Figure 33: Test series S07.AT. LHJ, comparisons between experimental and numerical force - displacement diagrams of a masonry wall subjected to uniaxial compression loading/unloading in the direction normal to head joints.

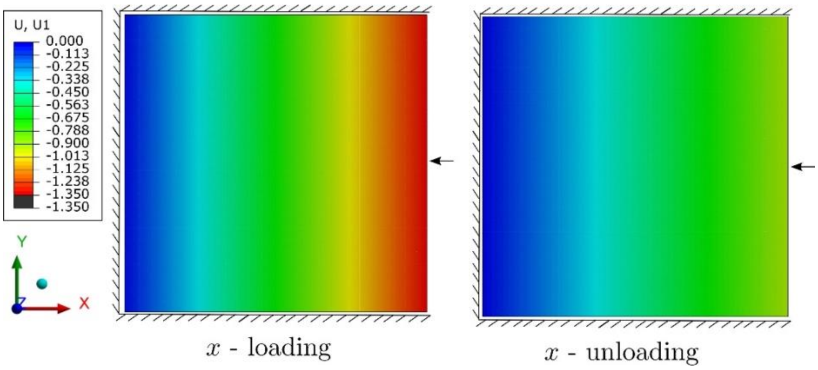

Figure 34: Test series S07.AT. LHJ: displacement fields (in mm), in the direction normal to head joints, of a masonry wall subjected to uniaxial compression loading/unloading in the direction normal to head joints (x direction) at maximum load level (left) and after unloading (right).

5.4 S08.AT.LBI: biaxial loading and unloading at room temperature

In this test series, two refractory masonry walls with dimensions 1100×1125×140 mm^3 were tested at room temperature. A 6 MPa biaxial compression load was applied to the directions normal to the bed and head joints at the same time. The FE models of the wall are similar to that presented in previous sections. The interactions between the contact surfaces of the wall, the plungers and the ground were considered in the FE model using frictional contact. The boundary conditions of the ground and the two fixed rigid plates are fully fixed.

5.4.1 Results from Micro-model

Figure 35 presents a comparison between the experimental and numerical force - displacement diagrams in the directions normal to bed and head joints during loading and unloading. The present numerical model can reproduce with reasonable accuracy the orthotropic displacement stiffening mechanical behaviour of the wall. The reaction force increases with the increase in the displacement due to the gradual closure of the joints and the increase in material stiffness with gradual closure of joints. The maximum displacement in the direction normal to the head joints is smaller compared to that in the direction normal to bed joints as the number of head joints is less than the number of bed joints.

Figure 36a makes the same observation as in Series S07.AT. LHJ-S08.AT.LBI where bricks behave almost as rigid units for low level of stress. Figure 36b shows the distribution of von Mises stresses at the first peak load. From the figure it is possible to observe that the stress is distributed uniformly at 6 MPa in the bricks except at areas near the support (right side of the figure) and the head joints. This is a combination of the stresses observed in the previous tests S07.AT. LHJ-S08.AT.LBI.

European Commission
Horizon 2020
European Union funding
for Research & Innovation

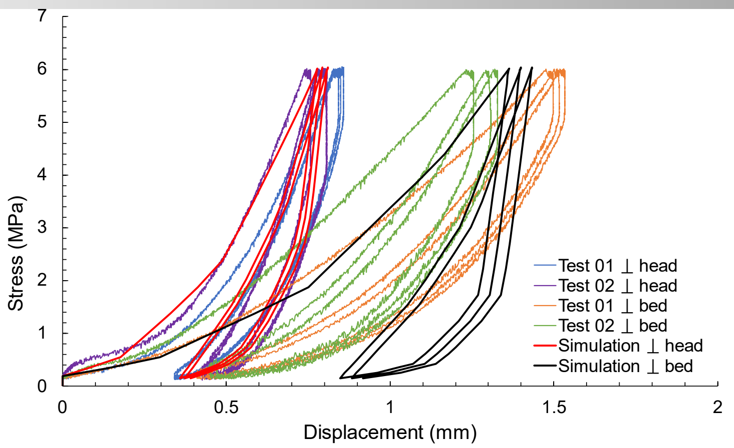

Figure 35: Test series S08.AT.LBI, comparisons between experimental and numerical force - displacement diagrams of a masonry wall subjected to biaxial compression loading/unloading in the directions normal to bed and head joints.

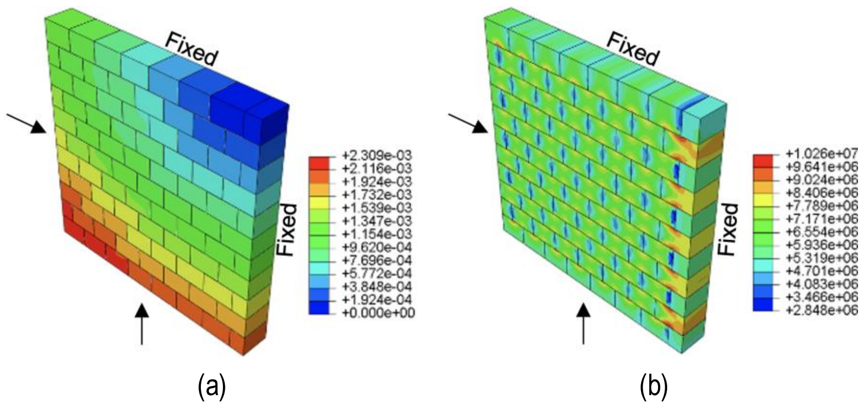

Figure 36: Test series S08.AT.LBI, a) displacement distribution (mm) and b) Von Mises stress distribution (Pa).

5.4.2 Results from Macro-model

Comparisons between the experimental and numerical force - displacement diagrams in the directions normal to bed and head joints during loading and unloading are presented in Figure 37. The present numerical model can reproduce with reasonable accuracy the orthotropic displacement stiffening mechanical behaviour of the wall. The reaction force increases with the increase in the displacement due to the gradual closure of the joints and the increase in material stiffness with gradual closure of joints. The maximum displacement in the direction normal to the head joints is smaller compared to that in the direction normal to the bed joints as the number of head joints is less than the number of bed joints.

The displacement fields in the direction normal to bed and head joints at maximum load level and after load removal are given in Figure 38. The arrows indicate the locations of the moving plungers (in the x- and y-directions) and the lines denote the positions of the two fixed rigid plates. After unloading, the wall did not return to the initial configuration and there was permanent deformation in both directions caused by gradual closure of joints, the deformation and the crushing of the asperities present at the contact surfaces of bed and head joints.

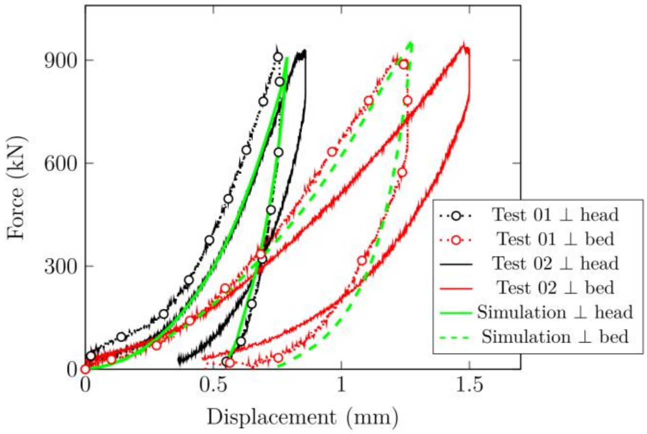

Figure 37: Test series S08.AT.LBI: comparisons between experimental and numerical force - displacement diagrams of a masonry wall subjected to biaxial compression loading/unloading in the directions normal to bed and head joints.

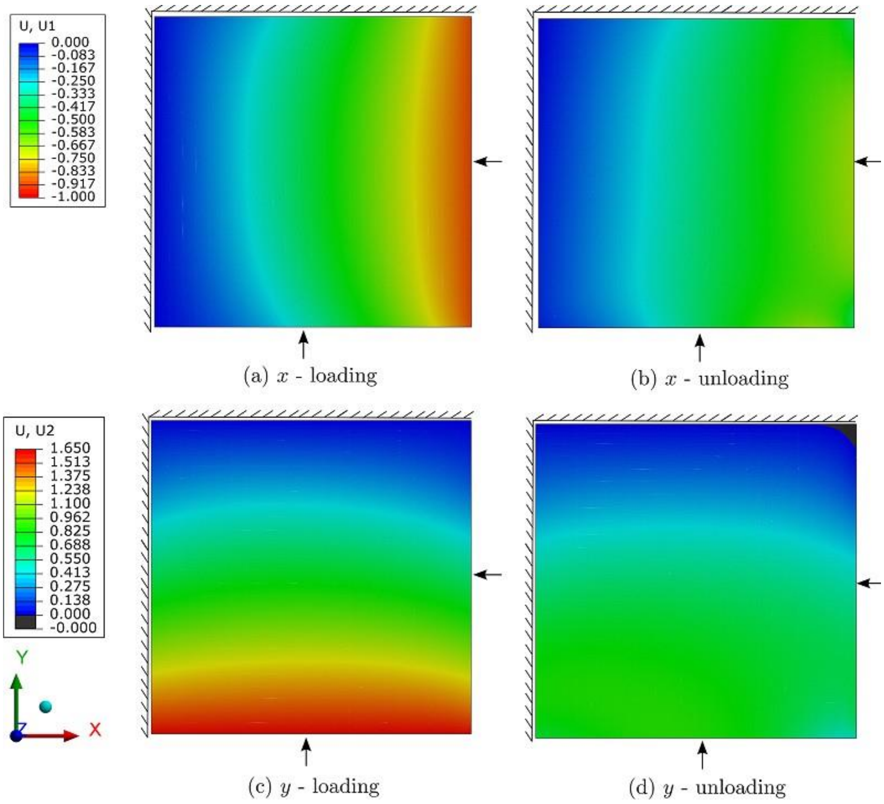

Figure 38: Test series S08.AT.LBI: displacement fields (in mm) in the direction normal to head joints (x direction, a and b) and in the direction normal to bed joints (y direction, c and d) at maximum load level (left) and after load remo val (right) of a masonry wall subjected to biaxial compression loading/unloading.

5.5 S09.HT.CBJ: uniaxial creep behaviour - normal to bed joints

Preliminary test was the first high temperature test, and it includes only one test. The main goal of this trial series was to test the high temperature test setup. Time variations of the wall's cold (CF) and hot (HF) face temperatures during heating and testing are presented in Figure 39**Error! Reference source not found.**. It can be seen that the temperature of the HF did not reach the desired value (1500 °C) due to low heating power provided by the heating system, high heat capacity of wall and the test setup, and high heat losses (from the heating hood to the ambient and the sides of the wall to the water-cooled plungers). The solid black lines in the figure represent the values measured by the thermocouples.

The FE analysis for this test was carried out only using the macro-modelling approach. The analysis of the wall compromises two steps: firstly, transient heat transfer analysis to compute the temperature distributions and variations with time and secondly, transient thermo- mechanical analysis to compute the thermomechanical stress and strain fields. The temperature fields calculated in the first step were used as a temperature load in the thermomechanical analysis. The heat transfer and thermomechanical FE models of the wall were developed using Abaqus. The physical model of the wall is similar to that of S06.AT (Figure 25b). The average measured temperature variations with time of the HF and CF are applied as thermal boundary conditions in the heat transfer analysis. Comparisons between the experimental and numerical CF and HF temperature variations with time are given in Figure 40**Error! Reference source not found.**. It should be mentioned that the obtained temperature variations of the HF and CF with time are, in fact, the applied temperature boundary conditions. The goal was to compute the temperature distributions and variations with time through the thickness of the wall.

Regarding the thermomechanical analysis, the four ceramic plates, as well as the top insulation layer (ground) of the test setup have been modelled as rigid plates. The wall (bricks and joints) was replaced by a homogeneous material whose mechanical properties depend on the state of the bed and head joints (open or closed). The frictional interactions between the contact surfaces of the wall and the fixed, moving rigid plates and the ground were considered (coefficient of friction of 0.5). During heating, load application and load holding steps, the boundary conditions of two fixed rigid plates and the ground are fully fixed. During heating, the two moving rigid plates were free to move then, during load application and load holding steps, the measured experimental reaction forces were applied as concentrated loads to the moving rigid plates.

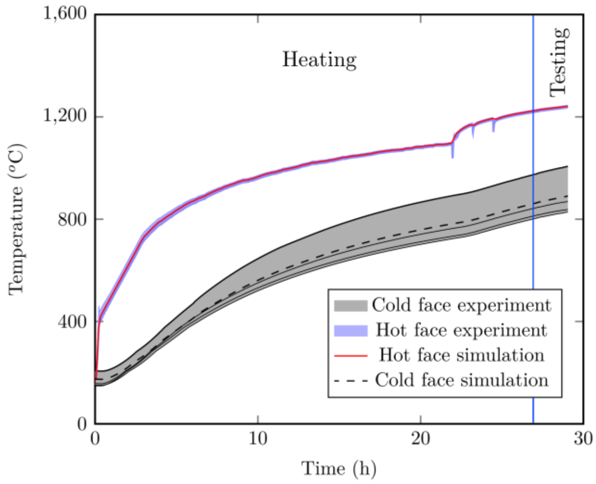

Figure 39: Preliminary test, time variations of the cold and hot faces temperatures during heating and testing, experimental and numerical results.

Comparisons between the experimental and numerical displacement - time diagrams during the loading and holding steps are given in Figure 40a. A good agreement between the experimental and numerical results were obtained. During loading, a steady increase in the displacement can be observed. Then, during the holding step, a slight increase in the displacement can be observed due to creep. The measured displacements are higher as compared to S06.AT. LBJ due to the low values of Young's modulus at high temperature and creep. The joint patterns in the wall by the end of load holding step are presented in Figure 40b. The word "fixed" indicate the locations of the fixed plungers and the arrows denote the moving plungers. In the HF, all bed joints are closed, and all head joints are still open (pattern B). On the other hand, in the CF, all bed and head joints are open (pattern O).

Regarding test series S09.HT.CBJ, it was possible to heat the wall to the desired temperature (1500 °C) after adjusting the electrical configurations of the heating system, increasing the input power, and improving the insulation of the experimental setup. In this test series, two refractory masonry walls with dimensions 1100×1125×140 mm^3 were tested at high temperature. The solution domain used for both the modelling approaches were similar to models in previous sections (Figure 25) and the mechanical boundary conditions of the ground, fixed and moving plungers are like those of the preliminary test.

For the analysis, four ceramic plates, as well as the base of the test setup have been modelled as rigid plates. During heating, load application and load holding steps, the boundary conditions of two fixed rigid plates and the ground are fully fixed. During heating, the two moving rigid plates were free to move then, during load application and load holding steps, the measured experimental reaction forces were applied as concentrated loads to the moving rigid plates.

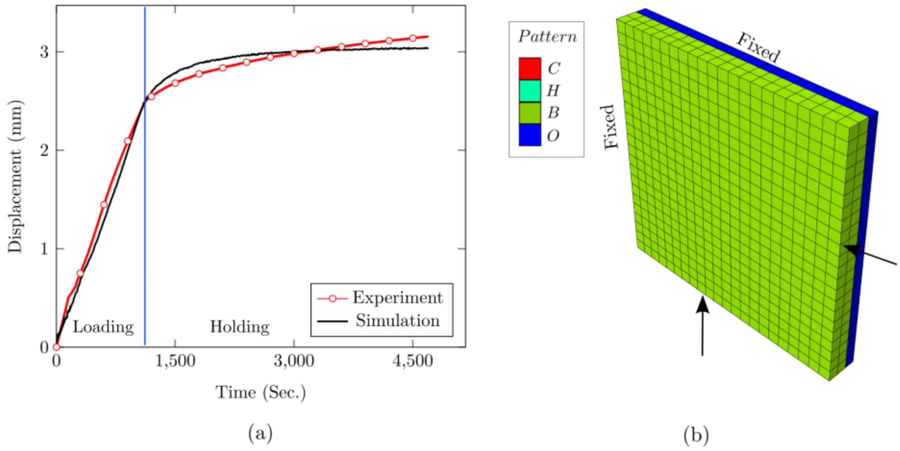

Figure 40: Preliminary test: (a) experimental and numerical time variations of the displacement in the direction normal to bed joints. (b) Joint patterns in the wall by the end of load holding step.

5.5.1 Results from Micro-model

Coupled thermal-displacement analysis was carried out for this simulation in which the wall was first subjected to gravity load, heating and then mechanical loads applied at high temperature. Thermal boundary conditions were used at the hot and cold faces of the model. The temperature values used for these boundary conditions are average values of the temperatures observed experimentally at those faces with thermocouples. Figure 41 presents the comparisons between the experimental and numerical HF and CF temperature variations with time. Figure 42 shows the temperature distribution in the wall. The temperature at the HF and CF are constant on the whole surface and within the wall, the temperature changes according to its thermal conductivity.

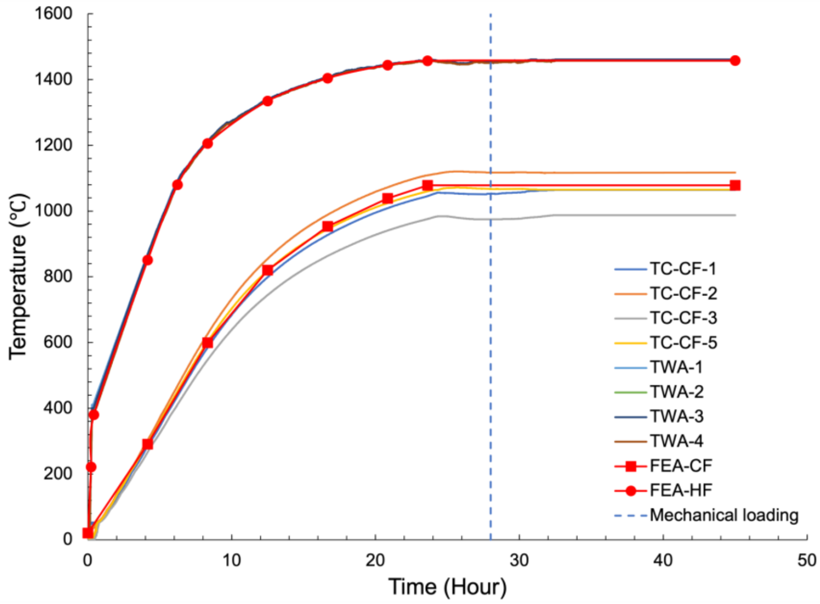

Figure 41: Test series S09.HT.CBJ, time variations of the cold and hot faces temperatures during heating and mechanical testing, experimental and numerical results

Figure 43a shows the comparison of stress-displacement profiles obtained experimentally and numerically. From the profile, it can be observed that values obtained numerically are in good agreement with the experimental results. It can be observed that, during the initial period of load application, there is a gradual increase in stiffness due to joint closing. The displacement is higher compared to the test performed at ambient temperature. This happens because of reduced Young's modulus and creep at high temperature. After the peak and during the holding, creep plays an important role as can be seen from Figure 43b. It can be observed from the figure that numerical profile of displacement-time is very similar to the profile achieved experimentally. Increase in displacement in the initial period is due to load application while an increase can be observed during holding due to creep. The slight difference between the experimental and numerical values are mainly due to the creep parameters. In this micro-modelling approach, only the primary creep parameters are used. This parameter lacks in showing the similar trend observed experimentally.

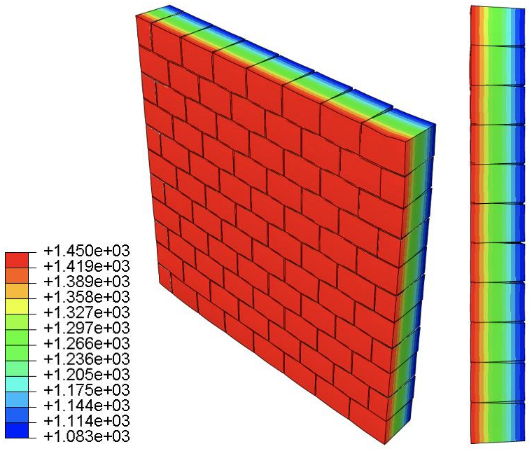

Figure 42: Test series S09.HT.CBJ, temperature distributions of the masonry wall by the end of heating step showing the deformation of the wall due to thermal expansion.

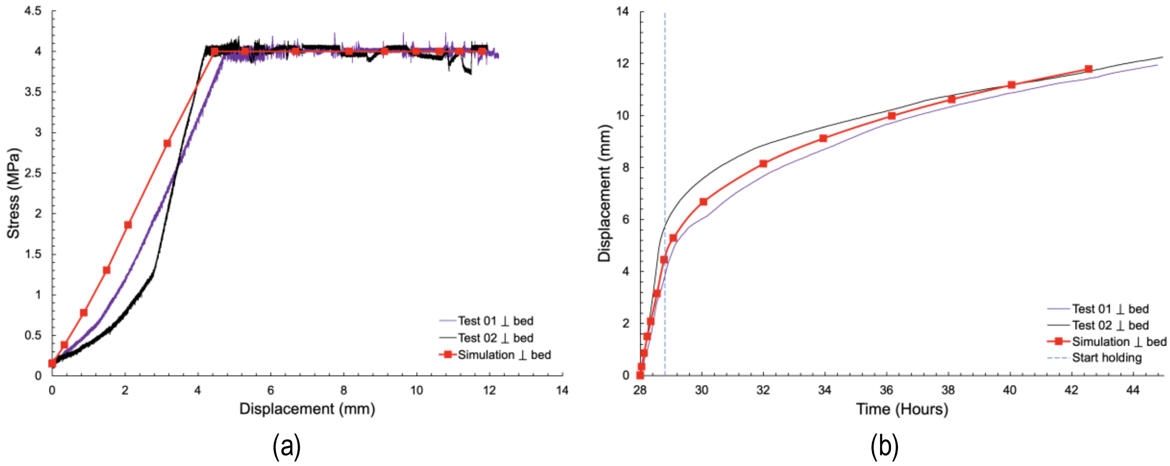

Figure 43: Test series S09.HT.CBJ, a) Stress-displacement profile and b) Displacement-Time profile.

Figure 44 shows the in-plane displacement profile for this test. From the figure it can be observed that at high temperature the bricks do not behave, largely, as rigid units as it was observed during the tests at ambient temperature. This is due to material property degradation and creep.

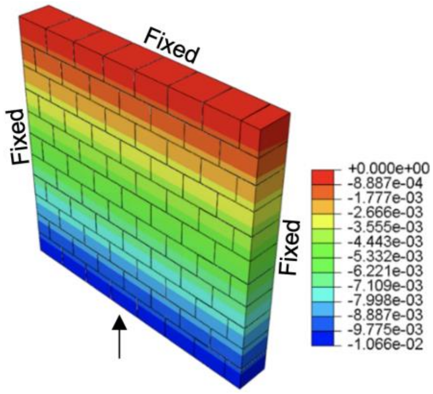

Figure 44: Test series S09.HT.CBJ: displacement distribution (mm).

5.5.2 Results from Macro-model

The analysis of the wall compromises two steps: firstly, transient heat transfer analysis to compute the temperature distributions and variations with time and secondly, transient thermo- mechanical analysis to compute the thermomechanical stress and strain fields. In the transient heat transfer analysis, the average measured temperature variations with time of the CF and HF were applied as thermal boundary conditions. The temperature fields of the wall during heating, load application, holding and unloading are obtained. These, in turn, are employed as thermal fields for the thermomechanical analysis. Comparisons between the experimental and numerical HF and CF temperature variations with time are given in Figure 45. The five solid black lines represent the temperatures measured by the thermocouples in contact with the CF.

The temperature field of the wall as well as the deformed shape, by the end of the heating step, due to thermal expansion effects are given in Figure 46. The word "fixed" denotes the locations of the fixed plungers while, the arrows indicate the positions of the moving plungers. Higher values of thermal deformation near the HF as compared to the CF can be observed from the figure due to the higher temperature of the HF. As a result, the sides of the wall (in contact with the moving and fixed plungers), were not perfectly parallel to the plunger linings (wedged shape, in the depth of the wall) before the load application.

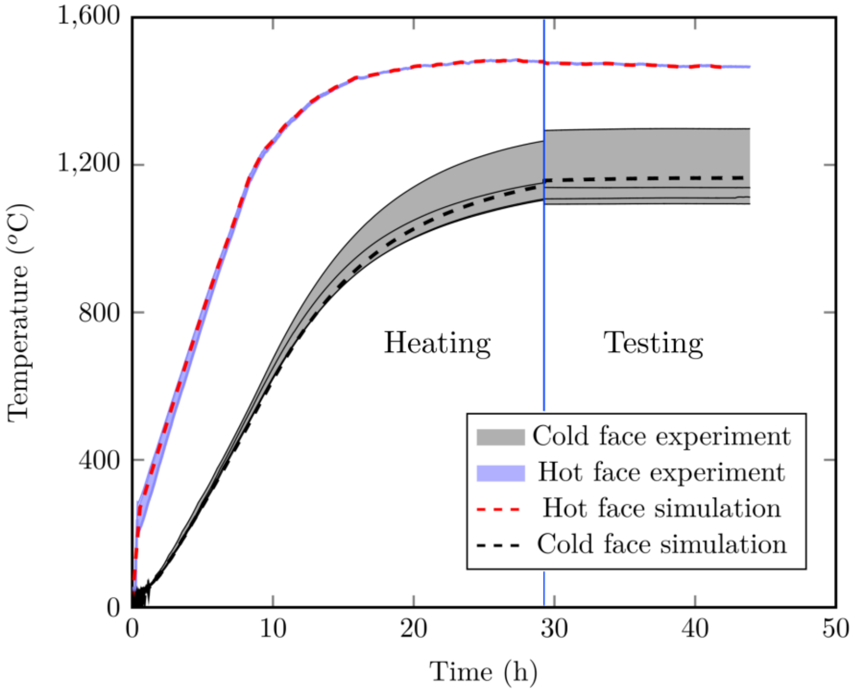

Figure 45: Test series S09.HT.CBJ: time variations of the cold and hot face temperatures during heating and mechanical testing, experimental and numerical results.

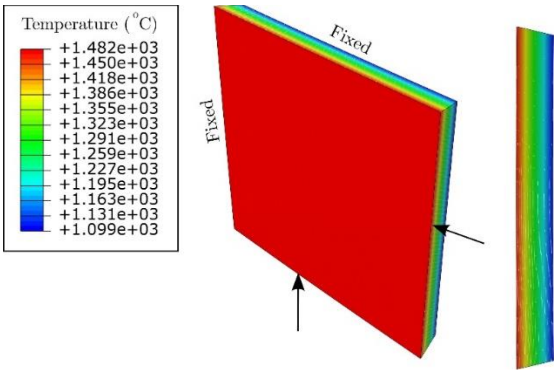

Figure 46: Test series S09.HT.CBJ: temperature distributions of the masonry wall by the end of heating step showing the deformation of the wall due to thermal expansion.

Figure 47-a presents comparisons between the experimental and numerical displacement - time diagrams during loading, holding and unloading steps. Good agreement between the numerical and the experimental results (the two performed tests in red) can be observed. During loading, a fast increase in the displacement can be observed due to gradual closure of joints with increasing applied load. Then, during the holding step, an increase in the displacement can be observed due to creep. Finally, the displacement decreased slightly during the unloading step. After load removal, the recovered displacement was very small as compared to the displacement due to the applied load. This can be attributed to the permanent deformation resulting from the viscoplastic behaviour of the structure and joints closure. By the end of the load application step, the displacement value is higher

compared to the preliminary test, due to the high bulk temperature of the specimen and, therefore, lower values of Young's modulus and higher creep rates.

Figure 47-b shows an example of time variations of the stresses (from the end of heating step to the end of unloading step) in the direction normal to bed joints (σ_{bed}), 15 millimetres from the HF and the CF. By the start of loading step, the HF carries almost all the applied load due to the wedged deformed shape of the wall (shown in Figure 46) caused by the thermal expansion and the temperature gradient through the thickness of the wall. With the increase of the applied load and the deformation of the zone near the HF, the contact area between the moving plungers and the sides of the wall started to increase and, therefore, the stresses in the CF as well. After reaching the maximum load level and due to the lower creep rate in the CF (due to the lower temperature) as compared to the HF, a decay in σ_{bed} HF was observed due to stress relaxation. In contrast, an increase in the σ_{bed} CF was observed and then, remained almost constant during the holding time.

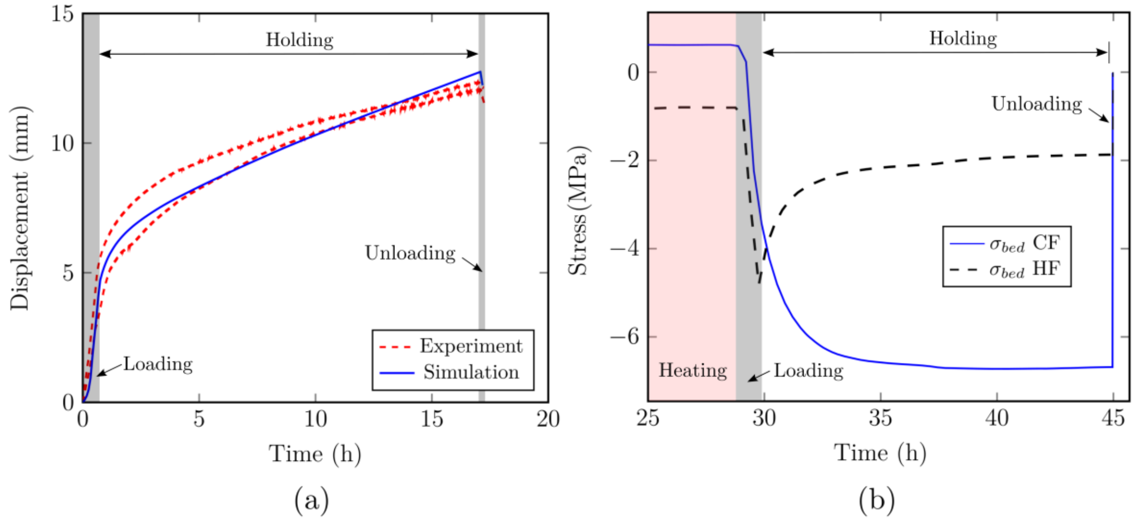

Figure 47: Test series S09.HT.CBJ, time variations of (a) displacement and (b) stresses in a masonry wall subjected to uniaxial creep load at 1450 °C in the direction normal to bed joints.

The joints pattern in the wall and the displacement in the loading direction (normal to bed joints) by the end of the holding step are presented in Figure 48. The word "fixed" indicates the locations of the fixed plungers and the arrows denote the moving plungers. In the HF, almost all bed and head joints are closed (pattern C). The closure of head joints is caused by the Poisson's effects and the creep (in direction normal to the loading direction). In the CF, almost all bed and head joints were closed while some head joints remained open (patterns C and B).

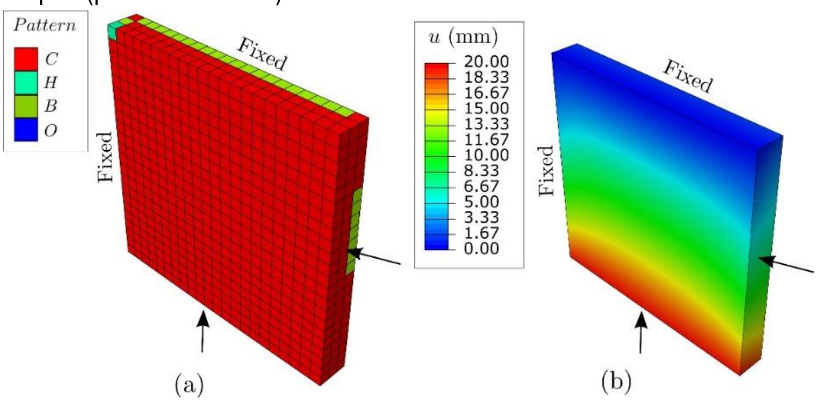

Figure 48: Test series S09.HT.CBJ, joint pattern and displacement fields in the direction normal to bed joints (vertical direction in this image) in a masonry wall subjected to uniaxial compression creep load at 1500 °C.

5.6 S10.HT.CBI: biaxial creep behaviour

In this test series, two refractory masonry walls with dimensions 1100×1125×140 mm^3 were tested at high temperature. The modelling technique of S10.HT.CBI is similar to that of S09.HT.CBJ for both the modelling approaches. During heating, load application, load holding and unloading steps, the boundary conditions of two fixed rigid plates and the ground are fully fixed.

European Commission | Horizon 2020 European Union funding for Research & Innovation

During heating, the two moving rigid plates were free to move then, during load application, load holding and unloading steps, the measured experimental reaction forces, in both directions, were applied as concentrated loads to the moving rigid plates.

5.6.1 Results from Micro-model

Figure 49a shows the comparison of stress-displacement profiles obtained experimentally and numerically. From the profile, it can be noticed that values obtained numerically are very similar to the experimental results. It can be observed that during the initial period of load application, there is a gradual increase in stiffness due to joint closure. The displacements in both directions are higher compared to the test performed at ambient temperature. This is due to reduced Young's modulus and creep at high temperature. After the peak and during the holding, creep plays an important role as can be seen from Figure 49b. It can be observed from the figure that numerical profiles of displacement-time are very similar to the profile achieved experimentally. Increase in displacement in the initial period is due to load application, while an increase can be observed during holding due to creep. The slight differences between the experimental and numerical values are mainly due to the creep parameters. In this micro-modelling approach only the primary creep parameters are used. This parameter lacks in showing the similar trend observed experimentally. Figure 50 shows the in-plane displacement profile for this test. From the figure, it can be observed that at high temperature the bricks do not behave, largely, as rigid units due to material property degradation.

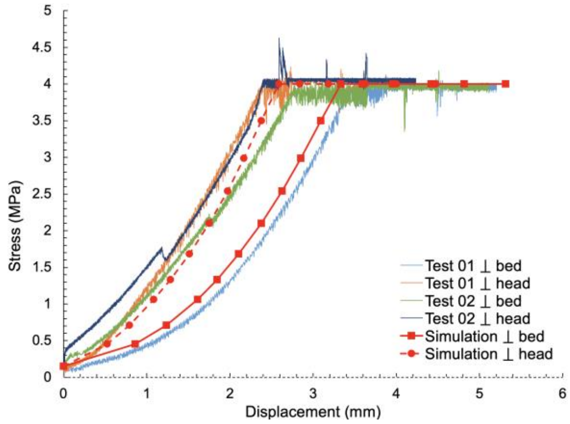

(a)

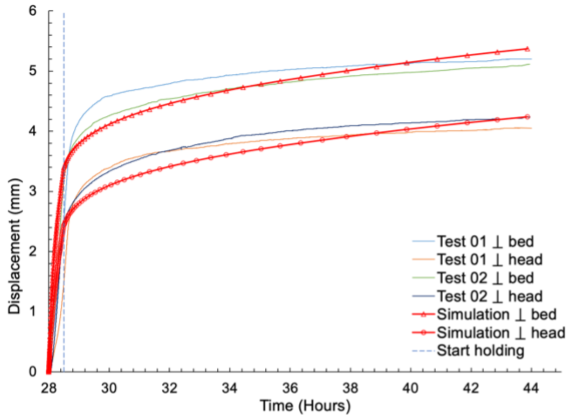

(b)

Figure 49: Test series S10.HT.CBI, a) Stress-displacement profile; b) Displacement-Time profile.

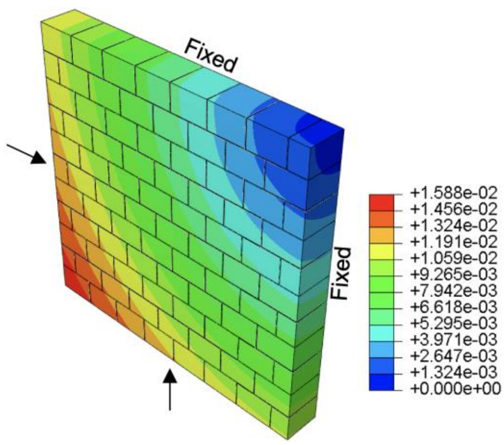

Figure 50: Test series S10.HT.CBI, displacement distribution (mm).

5.6.2 Results from Macro-model

Comparisons between the experimental and numerical displacement - time diagrams in the directions normal to bed and head joints during loading, holding and unloading steps are shown in Figure 51a. Good agreement between the experimental and numerical results can be observed. During load application step and for both directions, an increase in the displacement due to the gradual closure of joints can be observed. The maximum displacement in the direction normal to bed joints is higher as compared to that in the direction normal to head joints due to the difference between the number of bed and head joints in the wall.

An example of the time variations of the stresses (from the end of heating step to the end of unloading step) in the CF and HF in the direction normal to bed and head joints (σ_{bed} and σ_{head}) are reported in Figure 51-b. As compared to S09.HT.CBJ and S08, similar trends of σ_{bed} CF, HF and σ_{head} CF, HF can be observed. These trends can be explained in a similar way to that of series S09.HT.CBJ. The displacement in the loading directions and the joints pattern in the wall by the end of the holding step are shown in Figure 52 and Figure 53, respectively. The arrows denote the moving plungers and the words fixed indicate the locations of the fixed plungers. In the HF and CF, most of the bed and head joints are closed (pattern H). Some open bed and head joints near the fixed plungers can be seen.

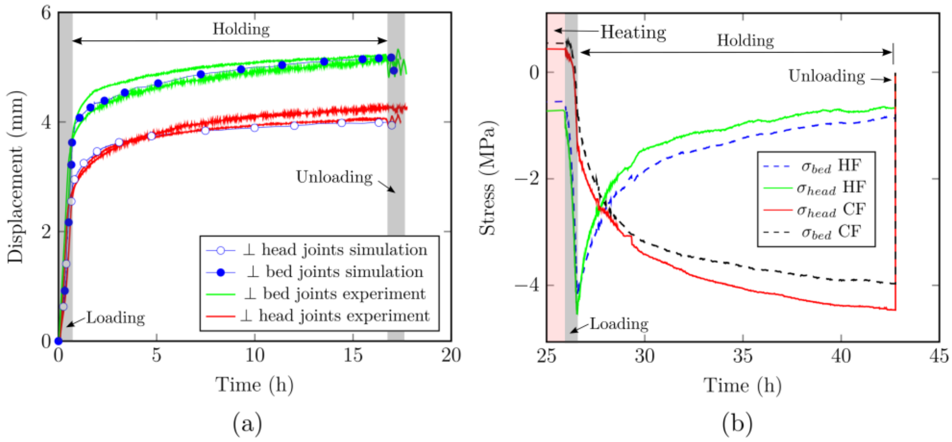

Figure 51: Test series S10.HT.CBI, time variations of (a) displacement and (b) stresses in a masonry wall subjected to biaxial creep load at 1450 °C.

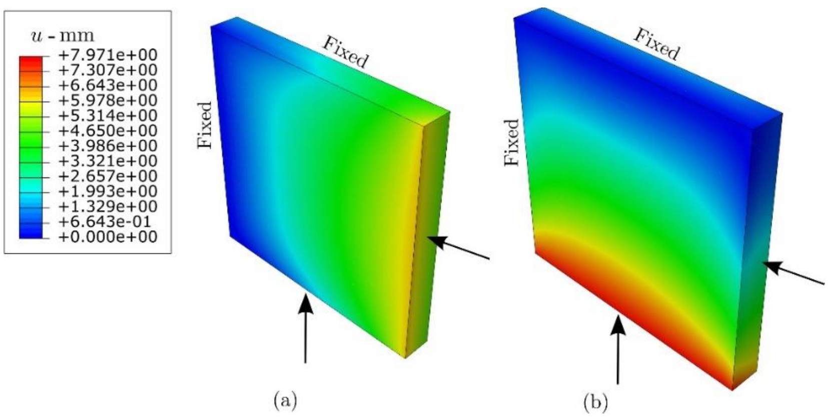

Figure 52: Test series S10.HT.CBI: displacement fields in a masonry wall subjected to biaxial compression creep load: (a) in the direction normal to head joints (horizontal direction in this image) and (b) in the direction normal to bed joints (vertical direction in in this image).

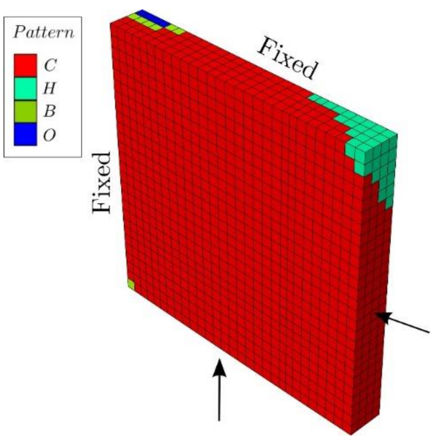

Figure 53: Test series S10.HT.CBI, joint pattern in a masonry wall subjected to biaxial compression creep load at 1500 °C.

5.7 S11.HT.RBI: biaxial relaxation behaviour

The goal of test series S11.HT.RBI was to investigate the relaxation behaviour of the wall (constant strain loading conditions). The modelling technique is similar to that of S09.HT.CBJ and S10.HT.CBI for both the modelling approaches. During heating, the mechanical boundary conditions of the plungers and the ground are similar to those of S10.HT.CBI. During loading, the boundary conditions are almost the same as S10.HT.CBI with only one difference, displacement boundary conditions were applied to the moving plungers and kept constant during the holding time.

5.7.1 Results from Micro-model

Comparisons between the experimental and numerical time variations of the resulting reaction forces, in the directions normal to bed and head joints, during the two loading cycles are reported in Figure 54. Good agreements between the experimental and numerical results can be observed. For this test series only the first cycle of the loading was performed numerically to observe the result with experimental results. During the experiment, in the first test, the first load cycle was for a duration of 6.5 hours while in the second test the duration of the cycle was increased to 15 hours. Therefore, to compare the numerical results with both the experimental outcomes, only the first load cycle with a duration of 6.5 hours was considered. During this cycle, the resulting reaction forces increased gradually to reach 600 kN. Subsequently, when the position of the plungers is locked, a decay in the resulting reaction forces was observed due to the relaxation behaviour of the wall. In the beginning of the holding stage, a significant decrease in the reaction forces can be observed.

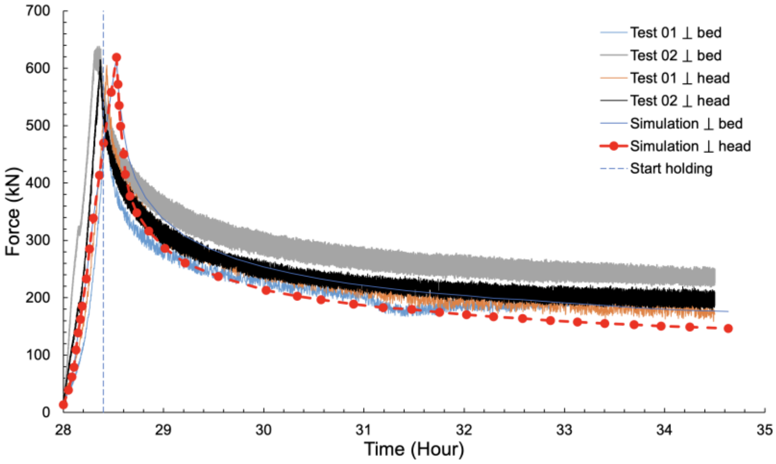

Figure 54: Test series S10, time variations of reaction forces.

5.7.2 Results from Macro-model

Comparisons between the experimental and numerical time variations of the resulting reaction forces, in the directions normal to the bed and head joints, during the two loading cycles are reported in Figure 55. Good agreements between the experimental and numerical results can be observed. During loading (1st cycle), the resulting reaction forces increased gradually to reach 600 kN. Then, when the position of the plungers is locked, a decay in the resulting reaction forces was observed due to the relaxation behaviour of the wall. In the beginning of the holding stage, a significant decrease in the reaction forces can be observed. Similar behaviour was noticed for both loading cycles.

The joints pattern in the wall by the end of the holding step and after unloading of the two loading cycles are presented in Figure 56. The arrows denote the moving plungers and the word “fixed” indicates the locations of the fixed plungers. It can be seen that some joints reopen after unloading. In addition, the percentage of the closed joints in the second loading cycle (Figure 56-c) is higher as compared to that of the first loading cycle (Figure 56-a). This can be attributed to the higher load applied to the wall in the second loading cycle as compared to that of the first loading cycle.

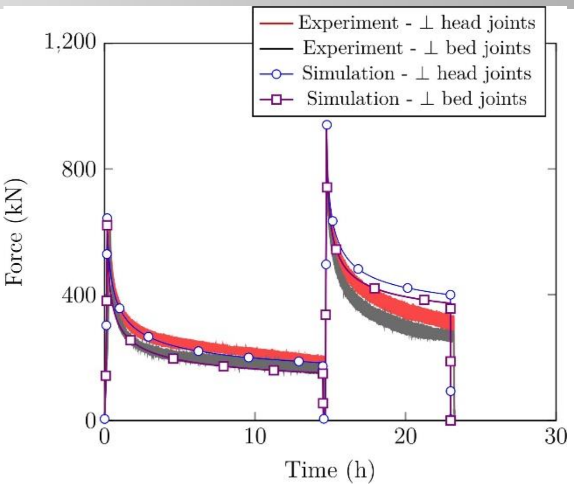

Figure 55: Test series S11.HT.RBI, time variations of reaction forces, in the directions normal to the bed and head joints, in a masonry wall subjected to a biaxial relaxation loading conditions at 1500 °C.

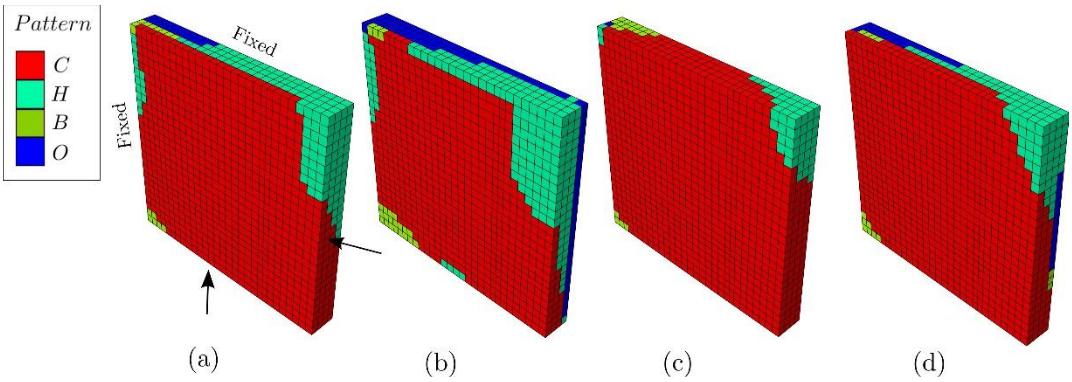

Figure 56: Test series S11.HT.RBI: joint patterns in a masonry wall subjected to biaxial relaxation: (a) after first loading, (b) after first unloading, (c) after second loading and (d) after second unloading.

6 Conclusions

This document presents the different numerical models to simulate the non-linear behaviour of the masonry sub-systems at ambient and high temperatures. These numerical simulations are necessary to calibrate different modelling approaches that can be later employed to validate an industrial system. In this document, two approaches are mentioned, homogenization approach and micro-modelling approach. The first one is developed at UORL, this approach replaces refractory brick units and dry joints with an equivalent homogenised material. The micro-modelling approach models both the units and joints between units. The results obtained from both these approaches, show a good agreement with the experimental results.

Both approaches can be used for the thermomechanical analyses of refractory structures. Depending on the outcome requirement, a particular approach can be selected. A homogenized model uses a simpler geometry modelling compared to micro-modelling, where all the individual units and interfaces must be modelled separately. This can be useful while modelling larger industrial structures. In general, compared to micro-models, homogenized models require less parameters to define the materials. In micro-models, additional parameters need to be defined, depending on the constitutive models used. While homogenized approach provides useful global outputs, micro-models can provide localised output as well (for example stress and strain concertation near the joints). The two approaches can be combined in a submodelling simulation: the displacement field obtained on an industrial vessel using the homogenization modelling will be used as boundary conditions on a little part of the vessel modelled using the micro-modelling to determine the “local” stresses.

7 References

[1] S. Samadi, S. Jin, D. Gruber, H. Harmuth, and S. Schachner, “Statistical study of compressive creep parameters of an

alumina spinel refractory," *Ceram. Int.*, vol. 46, no. 10, pp. 14662–14668, 2020, doi: 10.1016/j.ceramint.2020.02.267.
[2] D. Vitiello, "Thermo-physical properties of insulating refractory materials," Ph.D thesis, Université de Limoges, 2021.
[3] R. Kaczmarek, "Mechanical characterization of refractory materials," Ph.D thesis, Université de Limoges, 2021.
[4] R. L. G. Oliveira, J. P. C. Rodrigues, J. M. Pereira, P. B. Lourenço, and H. Ulrich Marschall, "Normal and tangential behaviour of dry joints in refractory masonry," *Eng. Struct.*, vol. 243, p. 112600, 2021, doi: 10.1016/j.engstruct.2021.112600.
[5] S. Russo and F. Sciarretta, "Masonry exposed to high temperatures: Mechanical behaviour and properties - An overview," *Fire Safety Journal*. 2013, doi: 10.1016/j.firesaf.2012.10.001.
[6] P. B. Lourenço, "Computational strategies for masonry structures," PhD-Thesis, TU Delft, 1996.
[7] G. G. Chewe Ngapeya, D. Waldmann, and F. Scholzen, "Impact of the height imperfections of masonry blocks on the load bearing capacity of dry-stack masonry walls," *Constr. Build. Mater.*, vol. 165, pp. 898–913, Mar. 2018, doi: 10.1016/J.CONBUILDMAT.2017.12.183.
[8] M. Ali, T. Sayet, A. Gasser, and E. Blond, "Transient Thermo-Mechanical Analysis of Steel Ladle Refractory Linings Using Mechanical Homogenization Approach," *Ceram. 2020, Vol. 3, Pages 171-189*, vol. 3, no. 2, pp. 171–188, Apr. 2020, doi: 10.3390/ceramics3020016.
[9] D. F. BV, "DIANA FEA Users' Manual - Release 10.3," 2019.
[10] M. Smith, *ABAQUS/Standard User's Manual, Version 2019*. United States: Dassault Systèmes Simulia Corp, 2019.
[11] J. Lubliner, J. Oliver, S. Oller, and E. Oñate, "A plastic-damage model for concrete," *Int. J. Solids Struct.*, vol. 25, no. 3, pp. 299–326, Jan. 1989, doi: 10.1016/0020-7683(89)90050-4.
[12] J. Lee and G. L. Fenves, "Plastic-Damage Model for Cyclic Loading of Concrete Structures," *J. Eng. Mech.*, vol. 124, no. 8, pp. 892–900, Aug. 1998, doi: 10.1061/(ASCE)0733-9399(1998)124:8(892).
[13] F. J. Vecchio and M. P. Collins, "The modified compression field theory for reinforced concrete elements subjected to shear," *ACI J.*, vol. 83, no. 22, pp. 219–231, 1986.
[14] R. G. Selby and F. J. Vecchio, *Three-dimensional Constitutive Relations for Reinforced Concrete*. Toronto: University of Toronto, Department of Civil Engineering, 1993.
[15] P. B. Lourenço, J. Rots, and J. Blaauwendraad, "Two approaches for the analysis of masonry structures," *Heron*, vol. 40, no. 4, pp. 313–340, 1995.
[16] C. A. Coulomb, "Essai sur une application des regles de maximis et minimis quelques problemes de statique, relatits a l'architecture," *Mem. Math. l'Academie R. Sci. 7*, 1776.
[17] M. Ali, T. Sayet, A. Gasser, and E. Blond, "Thermomechanical modelling of refractory mortarless masonry wall subjected to biaxial compression," in *UNITECR*, Oct. 2019, doi: 10.5281/zenodo.3574422.
[18] M. Ali, T. Sayet, A. Gasser, and E. Blond, "Computational Homogenization of Elastic-Viscoplastic Refractory Masonry with Dry Joints," *Int. J. Mech. Sci.*, vol. 196, p. 106275, Apr. 2021, doi: 10.1016/j.ijmecsci.2021.106275.
[19] T. M. H. H. Nguyen, E. Blond, A. Gasser, and T. Prietl, "Mechanical homogenisation of masonry wall without mortar," *Eur. J. Mech.*, vol. 28, no. 3, pp. 535–544, 2009, doi: 10.1016/j.euromechsol.2008.12.003.
[20] International Organization for Standardization, *ISO 834-1:1999 - Fire-resistance tests — Elements of building construction — Part 1: General requirements*. Switzerland, 1999.
[21] R. L. G. Oliveira, J. P. C. Rodrigues, J. M. Pereira, P. B. Lourenço, and H. U. Marschall, "Thermomechanical behaviour of refractory dry-stacked masonry walls under uniaxial compression," *Eng. Struct.*, vol. 240, no. December 2020, 2021, doi: 10.1016/j.engstruct.2021.112361.
[22] Y. A. Cengel and A. J. Ghajar, *Heat and mass transfer: fundamentals and applications*. McGraw-Hill Education, 2007.
[23] European Committee for Standardisation, *EN 1996-1-2. Eurocode 6 – Design of masonry structures, Part 1-2: General rules Structural Fire Design*. Belgium, 2005.

European Commission
Horizon 2020
European Union funding
for Research & Innovation